This peer-reviewed article has been accepted for publication in Publications of the Astronomical Society of Australia but not yet copyedited or typeset, and so may be subject to change during the production process.

The article is considered published and may be cited using its DOI. 10.1017/pasa.2025.10115

GLEAM-300: The GaLactic and Extragalactic All-sky Murchison Widefield Array (GLEAM) survey at 300 MHz

S. W. Duchesne, ¹ J. H. Cook, ² N. Hurley-Walker, ² A. J. M. Thomson, ¹ S. Paterson, ² C. J. Riseley, ³ S. J. McSweeney, ² S. Mantovanini, ² G. Heald, ^{4,1} T. M. O. Franzen, ⁵ K. Ross, ² N. Seymour, ² R. B. Wayth, ^{2,6} and T. J. Galvin ¹

Author for correspondence: S. W. Duchesne, Email: Stefan.Duchesne@csiro.au.

Abstract

In this paper we present a wide-field radio survey at 300 MHz covering the sky from $-90^{\circ} \le \delta_{J2000} \lesssim +40^{\circ}$ using the Murchison Widefield Array (MWA). This 300-MHz survey follows the Galactic and Extragalactic All-sky MWA (GLEAM) survey, and provides an additional comparatively high-frequency data point to existing multi-frequency (72–231 MHz) data. With this data release we provide mosaic images and a catalogue of compact source components. We use two-minute snapshot observations covering 2015–2016, combining overlapping two-minute snapshot images to provide full-sensitivity mosaic images with a median root-mean-square noise of $9.1^{+5.5}_{-2.8}$ mJy beam⁻¹ and median angular resolution of $128''.8 \times 112''.5$, with some position-dependent variation. We find a total of 338 080 unique Gaussian components across the mosaic images. The survey is the first at 300 MHz from the MWA covering the whole Southern Hemisphere. It provides a unique spectral data point that complements the existing GLEAM survey and the ongoing GLEAM-eXtended survey, and points toward results from the upcoming SKA-Low surveys.

Keywords: techniques: interferometric; galaxies: general; radio continuum: general; surveys

1. Introduction

The Murchison Widefield Array ^a (MWA; Tingay et al., 2013) is a low radio frequency aperture array located on Inyarrimanha Ilgari Bundara, the CSIRO ^b Murchison Radio-astronomy Observatory. The MWA operates from 72–300 MHz, and among its myriad science activities has been completing widefield, multi-frequency surveys in the form of the Galactic and Extragalactic All-sky MWA survey (GLEAM; Wayth et al., 2015).

GLEAM has resulted in five major data releases: the first all-sky extra-galactic images and extra-galactic catalogue (GLEAM EGC; Hurley-Walker et al., 2017), the Galactic plane between Galactic longitudes of $345^{\circ} < l < 60^{\circ}$ and $180^{\circ} < l < 240^{\circ}$ (Hurley-Walker et al., 2019), the South Galactic Pole (GLEAM SGP; Franzen et al., 2021), as well as circular polarization (Lenc et al., 2018) and linear polarization reprocessing (the POlarised GLEAM Survey; Riseley et al., 2018, 2020). The successor survey GLEAM-eXtended has also produced three data releases so far (GLEAM-X DR1 and DR2; Hurley-Walker et al., 2022a; Ross et al., 2024, and DR3 covering the Galactic Plane; Mantovanini et al., in press.) making use of the 'extended' baseline configuration of the Phase II MWA (Wayth et al., 2018). While GLEAM and GLEAM-X cover 72–231 MHz, the MWA bandpass extends beyond 300 MHz. Frequencies between 242-272 MHz are

Observations from the MWA at 300 MHz have posed a challenge in generating science-ready images. This is in part due to the antenna spacing and overall antenna design producing a primary beam response with significant grating lobes, contributing to overall lower sensitivity and differences in X and Y polarizations. With the intention to determine whether it would be feasible to process Phase I MWA observations at 300 MHz, Cook et al. (2021) showcased a processing pipeline that included careful modelling of the apparent brightness of sources for use in calibration, significant RFI flagging, and subtraction of sources in the primary beam grating lobes. These methods go beyond what is required to produce science-ready images for typical MWA observations below 230 MHz, but are generally applicable to all observations.

Many of the standard continuum data processing pipelines for the MWA have matured over the last few years, providing the ability to calibrate, image, and combine thousands of snapshot observations on supercomputing infrastructure. While there are still challenges that arise during processing (e.g. mysterious aliasing artefacts shown by Ross et al., 2024), the cur-

¹CSIRO Space and Astronomy, PO Box 1130, Bentley WA 6102, Australia

²International Centre for Radio Astronomy Research, Curtin University, Bentley, WA 6102, Australia

³Astronomisches Institut der Ruhr-Universität Bochum (AIRUB), Universitätsstraße 150, 44801 Bochum, Germanv

⁴SKA Observatory, SKA-Low Science Operations Centre, 26 Dick Perry Avenue, Kensington, WA 6151, Australia

⁵SKA Observatory, Jodrell Bank, Lower Withington, Macclesfield SK11 9FT, UK

⁶SKA Observatory, Science Operations Centre, CSIRO ARRC, 26 Dick Perry Avenue, Kensington, WA 6151, Australia

occupied by radio frequency interference (RFI) from known satellites (Sokolowski et al., 2016) and are avoided. Beyond $\approx 280\,\text{MHz}$, RFI occupancy drops sufficiently to provide a usable 'high'-frequency band and from 2015–2016 the Phase I MWA was used to perform another all-sky survey, based on the successful GLEAM drift-scan observing strategy, this time at 300 MHz.

^ahttps://www.mwatelescope.org/.

^bCommonwealth Scientific and Industrial Research Organisation.

[©] The Author(s), 2025. Published by Cambridge University Press on behalf of Astronomical Society of Australia. This is an Open Access article, distributed under the terms of the Creative Commons Attribution licence (https://creativecommons.org/licenses/by/4.0/), which permits unrestricted re-use, distribution and reproduction, provided the original article is properly cited.

rent generation of MWA data processing pipelines are able to image much of the data with only minor user intervention. Within the context of surveys, we have the GLEAM-X pipeline ^c (Hurley-Walker et al., 2022a; Ross et al., 2024), which has been processing GLEAM-X on a variety of supercomputers, and the Deep Imaging Pipeline (DIP d), which is being used to process the MWA Interestingly Deep AStrophysical (MIDAS) survey (Paterson et al., submitted). On top of improvements to general calibration and imaging, the MWA All-Sky Virtual Observatory ^e (ASVO) provides both a user interface to interact with MWA archives and to then perform pre-processing on observations using the *Garrawarla* and *Setonix* supercomputers at the Pawsey Supercomputing Research Centre f, which can then be delivered ready for calibration to the user, or calibrated using existing bandpass and gain solutions derived from the observatory's daily calibrator scans (Sokolowski et al., 2020). With numerous upgrades to data (pre-/post-)processing since the original GLEAM survey was released, we have opted to revisit the heretofore unprocessed and unpublished 300 MHz MWA observations.

In the Southern Hemisphere to date there are no widefield surveys near 300 MHz matching the angular resolution and sensitivity of GLEAM, motivating us to progress this work. There are only a handful of surveys near 300 MHz, typically originating in the Northern Hemisphere, that provide some coverage. From radio interferometers these include The Texas Survey (hereinafter, TXS) of radio sources covering $-35.5^{\circ} < \delta < +71.5^{\circ}$ at 365 MHz (Douglas et al., 1996), Westerbork in the Southern Hemisphere (WISH; De Breuck et al., 2002) at 352 MHz with 54 arcsec \times 54 csc δ arcsec angular resolution, covering $-9^{\circ} < \delta < -26^{\circ}$, the Molonglo Reference Catalogue (hereinafter, MRC; Large et al. 1981) covering $-85.0^{\circ} < \delta_{B1950} < +18.5^{\circ}, |b| \ge 3^{\circ}$ at 408 MHz. More recently, the Karl G. Jansky Very Large Array (VLA) Low-band Ionosphere and Transient Experiment (VLITE g) is being used to produce a survey at 340 MHz as the VLITE Commensal Sky Survey (VCSS; Clarke et al., 2016; Polisensky et al., 2016; Peters et al., 2021). VCSS is a multi-epoch survey covering the sky above $\delta_{J2000} > -41.7^{\circ}$, with first epoch data products (VCSS1; Peters et al., 2022) showing an average angular resolution of $\approx 15'' \times 15''$ and root-mean-square (rms) noise of $\approx 3 \,\mathrm{mJy\,beam^{-1}}$. In addition to the interferometric surveys, the 'Low-Band South' component of the Global Magneto-Ionic Medium Survey (GMIMS-LBS, Wolleben et al., 2019) covers 286.25 to 487.75 MHz and $-90 < \delta_{J2000} < +20^{\circ}$, using Murriyang, CSIRO's Parkes radio telescope. Being a single dish survey, its angular resolution is coarse (81–45') but is sensitive to all angular scales down to the resolution element.

This paper describes the GLEAM 300 MHz survey in detail,

named GLEAM-300, detailing the data processing for the individual observations (Section 2), combining the data products to produce science-ready images (Section 3) and a compact source catalogue (Section 4), and finally a discussion about applications and future work (Section 5). The catalogue and images are publicly released alongside this paper. We define a spectral index, α , via $S_{\nu} \propto \nu^{\alpha}$ for a flux density S_{ν} at frequency ν . Asymmetric uncertainties are reported at the 16-th and 84-th percentile unless otherwise noted.

2. 300 MHz observations and data processing

Observations for the 300-MHz GLEAM survey follow the same drift-scan observing strategy used for GLEAM and GLEAM-X. This observing mode has the telescope form a primary beam near the meridian towards a given declination, and takes twominute snapshots as the sky drifts above the observatory over the course of an observing night. Due to the smaller fieldof-view (FoV) of the MWA at 300 MHz, extra declinations are used to ensure uniform sensitivity, resulting in 13 declination strips from $-72.0^{\circ} \lesssim \delta_{\rm J2000} \lesssim +18.6^{\circ}$. These observations provide primary beam mainlobe sensitivity from $-80^{\circ} \lesssim \delta_{\rm J2000} \lesssim +24^{\circ}$. The declination strips and observation dates are summarised in Table 1. The observations have 30.72 MHz bandwidth (covering 284.8–315.5 MHz), and were recorded at 40 kHz/0.5 s frequency/time resolution, following the original GLEAM. Individual observations are referred to by unique observation IDs (ObsIDs) defined by the start time in GPS time format.

GLEAM 300 MHz data processing follows standard continuum snapshot processing strategies. In this case, we follow the processing strategy used by Duchesne et al. (2020) h. Data are pre-processed through the ASVO, which includes automated flagging with AOFlagger (Offringa et al., 2012, 2015) and averaging to 4 s time resolution. In the following sections, we briefly describe the processing with particular emphasis on differences between GLEAM/GLEAM-X and GLEAM 300 MHz. All two-min snapshots are pre-processed, calibrated, imaged, and post-processed individually prior to mosaicking and final source-finding activities described in later sections.

2.1 Calibration and flagging

Figure 1 shows example primary beam attenuation patterns (with main, grating, and side lobes) for a zenith scan [pointed towards declination -26.7° , 1(i)] and a low-elevation scan [pointed towards declination $+18.6^{\circ}$, 1(ii)] with the pointing directions indicated by green stars. The main lobe is closest to the pointing direction, but at this frequency and particularly for low elevations, the grating lobes approach the sensitivity of the main lobe. Cook et al. (2021) used observations of bright 'calibrator' sources to ensure bandpass and direction-independent complex gains can be solved when the primary beam grating lobes contribute significant amounts of power. We found that

^chttps://github.com/GLEAM-X/GLEAM-X-pipeline.

^dhttps://github.com/sjpaterson/dip.

ehttps://asvo.mwatelescope.org/.

fhttps://pawsey.org.au/. Garrawarla was decomissioned at the beginning of 2025 after providing over four years of excellent service to the MWA Collaboration. ASVO pre-processing is now done using dedicated resources on the the Pawsey Supercomputing Research Centre cluster Setonix.

ghttps://vlite.nrao.edu/

^hUsing the 'Phase II Pipeline' (piip): https://gitlab.com/Sunmish/piip, though note despite the name the pipeline is also suitable for processing MWA Phase I data as is the case here.

Table 1. Declination strips and observation information.

Declination	Dates	$N_{snapshots}$	Solutions type ^a	Median rms ^b	Good snapshots
(°)		•	(C / N / S)	$({ m mJybeam^{-1}})$	(%)
+32.0	2015 Sep 15, Nov 06, Dec 12; 2016 Feb 15, Apr 19, Jun 23	1877	39% / 34% / 27%	128^{+43}_{-30}	84%
+23.0	2015 Sep 16, Nov 07, Dec 13; 2016 Feb 16, Apr 20, Jun 24	939	0% / 55% / 45%	75^{+37}_{-17}	84%
+18.6	2015 Sep 21, Nov 12, Dec 19; 2016 Feb 21, Apr 26, Jun 30	922	34% / 48% / 18%	64^{+29}_{-14}	85%
+9.7	2015 Sep 21, Nov 12, Dec 19; 2016 Feb 21, Apr 26, Jun 30	921	23% / 71% / 7%	55^{+19}_{-10}	86%
+1.6	2015 Sep 20, Nov 11, Dec 18; 2016 Feb 20, Apr 25, Jun 28	936	62% / 10% / 29%	57^{+31}_{-14}	77%
-5.9	2015 Sep 20, Nov 11, Dec 18; 2016 Feb 20, Apr 25, Jun 28	933	48% / 42% / 10%	60^{+26}_{-19}	82%
-13.0	2015 Sep 19, Nov 10, Dec 22; 2016 Feb 19, Apr 24, 27, Jun 27	1026	72% / 13% / 15%	51 ⁺²⁶	66%
-19.9	2015 Sep 19, Nov 10, Dec 22; 2016 Feb 19, Apr 24, 27, Jun 27	1025	7% / 53% / 40%	55^{+19}_{-11}	86%
-26.7	2015 Sep 15, Nov 06, Dec 12; 2016 Feb 15, Apr 19, Jun 23	1877	40% / 33% / 27%	56^{+13}_{-13}	85%
-33.5	2015 Sep 16, Nov 07, Dec 13; 2016 Feb 16, Apr 20, Jun 24	939	0% / 51% / 49%	49 ⁺²³	72%
-40.4	2015 Sep 16, Nov 07, Dec 13; 2016 Feb 16, Apr 20, Jun 24	940	8% / 59% / 33%	52^{+21}_{-11}	86%
-47.5	2015 Sep 17, Nov 08; 2016 Feb 17, Apr 21, Jun 22	800	0% / 87% / 13%	59^{+20}_{-17}	84%
-55.0	2015 Sep 17, Nov 08; 2016 Feb 17, Apr 21, Jun 22	799	4% / 77% / 19%	66^{+29}_{-25}	87%
-63.1	2015 Sep 18, Nov 9, Dec 16; 2016 Feb 18, Apr 23, Jun 26	837	9% / 75% / 16%	62^{+35}_{-21}	78%
-72.0	2015 Sep 18, Nov 9, Dec 16; 2016 Feb 18, Apr 23, Jun 26	837	8% / 70% / 22%	72^{+15}_{-21}	79%
-76.0	2015 Sep 19, Nov 10, Dec 22; 2016 Feb 19, Apr 24, 27, Jun 27	1025	6% / 54% / 39%	90 ⁺³⁴	86%
-86.0	2015 Nov 06, Dec 12; 2016 Feb 15, Apr 19, Jun 23	1877	39% / 32% / 29%	150^{+56}_{-29}	82%
All	-		26% / 48% / 26%	68 ⁺⁵⁹	83%

^a 'C': solutions derived from a dedicated calibrator scan; 'N': nearest-in-time best solutions from other observations; 'S': solutions derived from the observation itself.

^b Median rms noise in a single two-minute snapshot image after applying the brightness scale correction described in Section 2.4.3.

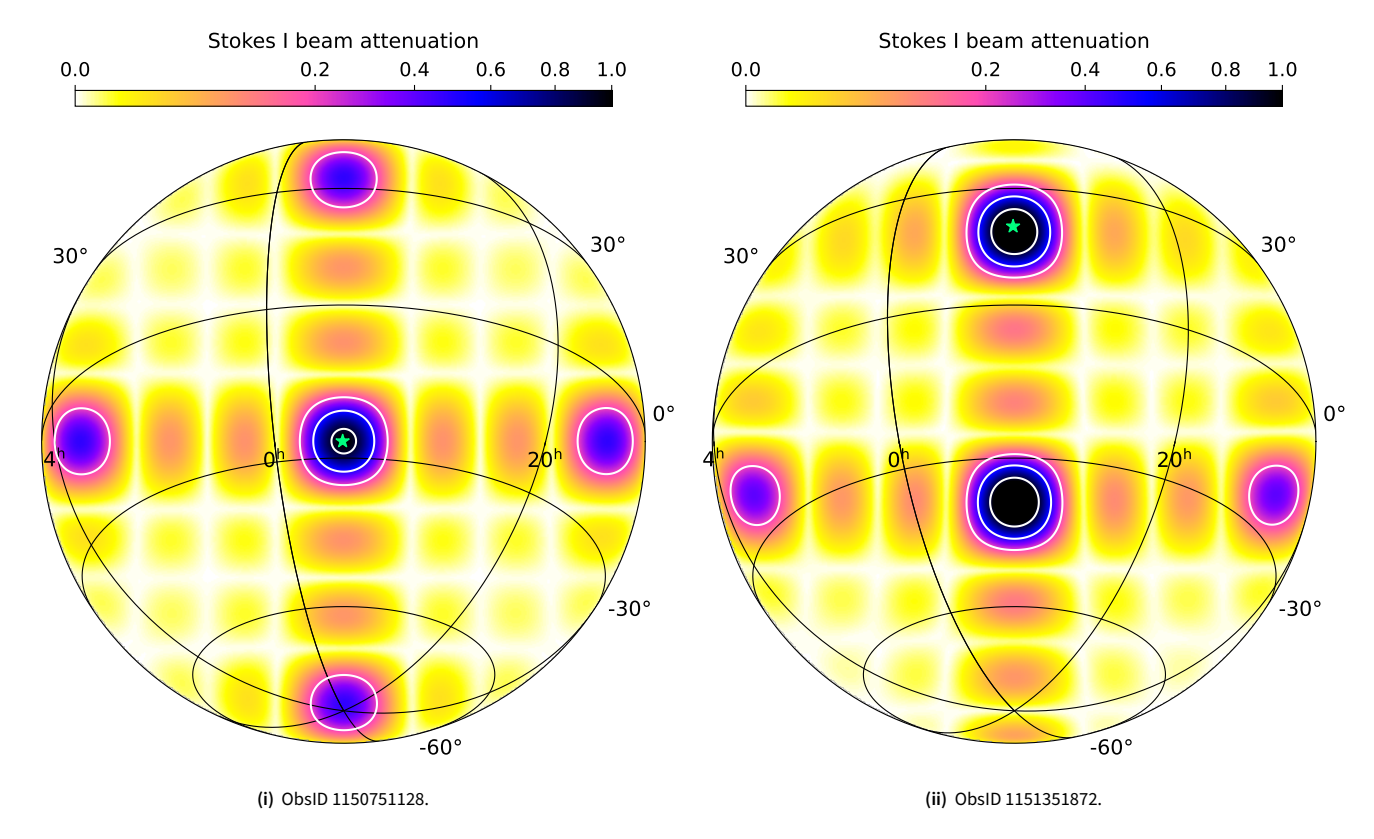


Figure 1. Example primary beam response for a zenith pointing [declination -26.7° , (ii)] and a low-elevation pointing [declination $+18.6^{\circ}$, (ii)]. The attenuation is displayed with square-root stretch, and the white contours trace [0.2, 0.5, 0.9]. The green stars indicate the main lobe, in the pointing direction, and significant grating lobes are those above the 0.2 contour.

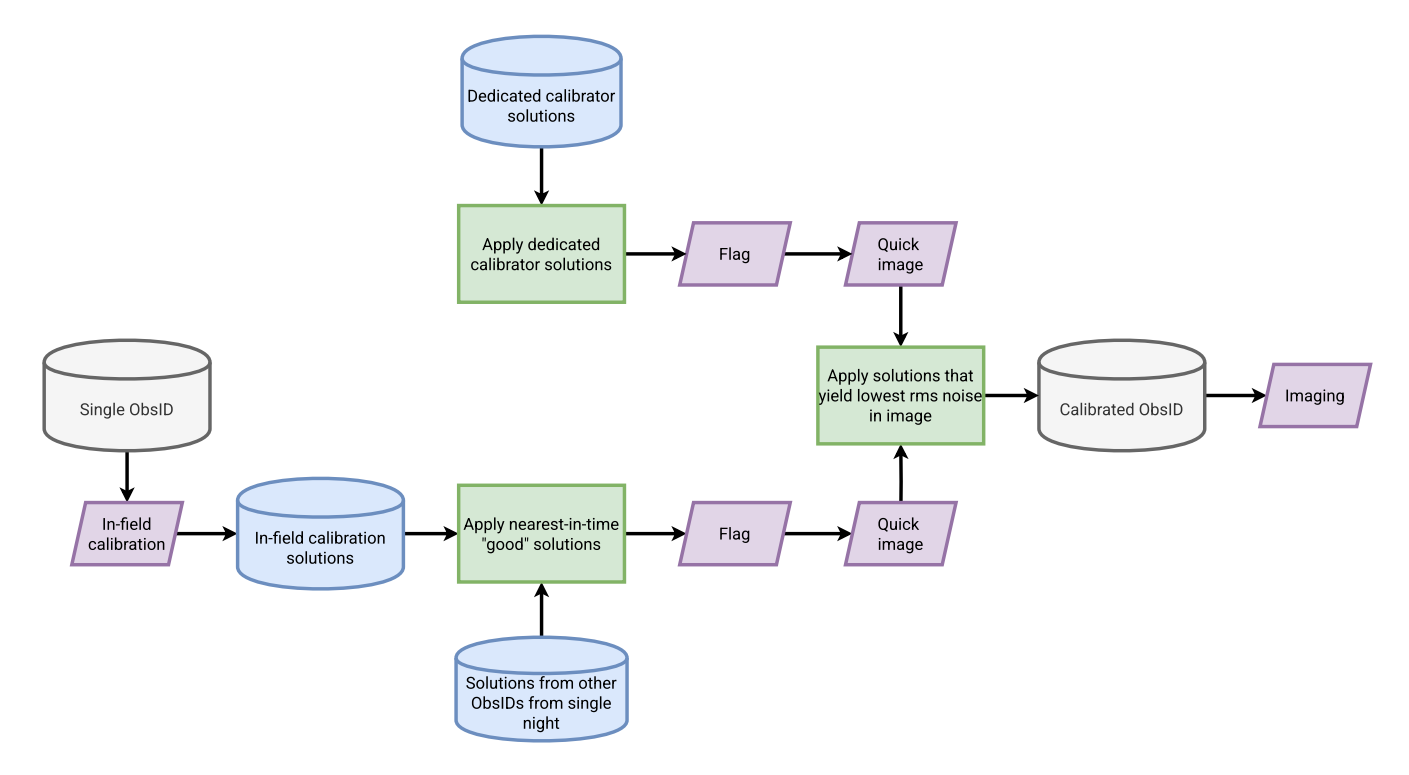


Figure 2. Flow diagram of the calibration procedure. The diagram shows the processing steps to assign good calibration solutions to each ObsID after initial pre-processing, and prior to peeling/outlier source subtraction, and imaging.

following this approach presented two issues: (1) we were unable to achieve good calibration solutions for some dedicated calibrator scans for unknown reasons, and (2) the gains drift over the course of the night and good calibration solutions become less effective as the night progresses. The alternate approach being used in other MWA processing strategies is to perform in-field calibration for every snapshot observation (e.g. Franzen et al., 2021, but see also Duchesne et al. 2020; Lynch et al. 2021; Hurley-Walker et al. 2022a). For these 300-MHz observations, the in-field approach suffers a higher failure rate than the dedicated calibrator scans, reducing to only 26% of observations arriving at good bandpass and gain solutions. In the context of these 300-MHz observations, 'in-field' refers to the main lobe as well as grating lobes above an attenuation of 20%. A local sky model is constructed for each observation from a subset of the GLEAM global sky model Hurley-Walker et al. (2022a) i. We take the 1 000 sources with the highest attenuated brightness using their frequency-dependent models. We note that while the sky model is largely based on GLEAM, the sky above $\delta_{\rm J2000} \gtrsim +30^{\circ}$ is filled in with sources from the NRAO ^j VLA Sky Survey catalogue (NVSS; Condon et al., 1998) at 1 400 MHz. These northern sources have a two-point spectral index that is derived after cross-matching to the VLA Lowfrequency Sky Survey redux catalogue (VLSSr; Lane et al., 2014) k at 74 MHz.

Our calibration process makes use of a mixture of in-field solutions and dedicated calibrator solutions, selecting solutions that reduce the image rms noise. This process is outlined in a flow diagram in Figure 2 and summarised as follows. We initially obtain calibration solutions from each nightly calibrator scan, using the same in-field calibration approach on the calibrator observation. We then apply the solutions to the survey ObsIDs, perform additional flagging, then create a shallow quick-look image.

Then, on uncalibrated data we perform in-field calibration with all ObsIDs. We then consider in-field solutions 'good' if they satisfy

- 1. $\sigma_{\text{amplitude}} < 40 \, \text{Jy}$,
- 2. $\sigma_{\text{phase}} < 2^{\circ}$,
- 3. < 35% solutions flagged from data that are not initially flagged,

where $\sigma_{amplitude}$ and σ_{phase} are the standard deviations of the amplitude and phase of the complex gains, checking both the XX and YY polarizations separately. We ignore XY and YX instrumental polarizations as we do not perform polarization calibration and assume all calibrators are unpolarized. Solutions identified as good are applied directly to their host snapshots, and for ObsIDs with 'bad' solutions the nearest-in-time good solution is applied with no interpolation. Another set of shallow quick-look images is then made after further flagging.

The two quick-look images are compared for each ObsID, and we record the set of solutions that produced the lowest rms noise in the image and use those solutions to calibrate the data. In Table 1 we note the fraction of ObsIDs for each

ⁱSee https://github.com/GLEAM-X/GLEAM-X-pipeline.

^jNational Radio Astronomy Observatory.

khttps://github.com/johnsmorgan/marco/tree/master/gleam_sky_model.

night that use either dedicated calibrator solutions ('C'), the in-field solutions derived from the ObsID itself ('S'), or the nearest-in-time in-field solutions ('N').

At multiple stages in the calibration process, prior to imaging, we perform a significant amount of RFI flagging. Alongside AOFlagger, we also follow Cook et al. (2021) and make heavy use of the automated flagging tasks rflag and tfcrop within the Common Astronomy Software Applications (CASA; CASA Team et al., 2022) 1 package. This is done before and after calibration. We also use the gain solutions to identify poorly-performing MWA tiles that are typically flagged for a given observing night. While the total percentage of flagged data varies between observations, we see approximately 60% of data flagged, which is a reasonable increase from the 20–30% normally seen at lower frequencies from other GLEAM observations processed with the same pipeline.

2.2 Imaging

2.2.1 Outlier source subtraction

Prior to imaging, we opt to peel and/or subtract a selection of sources outside of the primary beam mainlobe. We begin with peeling and subtraction of specific bright sources (e.g. Pictor A, Cygnus A—see Appendix B for a full list). This peeling process uses a model of the primary beam to estimate the apparent brightness of sources in this collection of bright sources, and if above 77 Jy at 300 MHz they are peeled and if above 2.3 Jy directly subtracted (without gain calibration) from the data ^m. We use the peeling pipeline PotatoPeel ⁿ (see Duchesne et al., 2023, for a description of the process), which uses the CASA package and WSClean (Offringa et al., 2014) o to generate image-based CLEAN component models of the apparent brightness of the source, which are used for amplitude and phase gain calibration before subtraction of the offending source as done in peeling (e.g. Smirnov, 2011). After removal of individual bright sources, we also image a selection of primary beam grating and side lobes in the order of attenuation (i.e. brightest lobe first). The CLEAN component models from the lobe images are subtracted to remove any additional contamination from off-axis sources. For most observations, a majority of the grating lobes are subtracted alongside a small number of side lobes.

2.2.2 Snapshot images

After outlier sources and grating/side lobes are subtracted, we make images of the main lobe covering approximately $21^{\circ} \times 21^{\circ}$. We make use of multi-scale deconvolution from WSClean (Offringa & Smirnov, 2017) and the w-gridder algorithm (Arras et al., 2021; Ye et al., 2022). For image weighting, we use the 'Briggs' weighting scheme (Briggs, 1995) with a robust parameter of 0. This weighting is chosen as it optimises

sensitivity without significant cost to angular resolution for these data. While some baselines end up flagged prior to imaging due to RFI and poor calibration, there is no explicit baseline or (u,v) cut added.

Initial imaging runs used automatic masking within WSClean, generating a mask once CLEANing reaches an initial global threshold of $3\sigma_{\rm rms}$, and then continuing down to $1\sigma_{\rm rms}$ within the derived mask. We found that this approach introduced a bias in flux density measurements of sources below the initial masking threshold. We suspect that too many noise components were deconvolved and may have redistributed flux away from un-deconvolved sources. We detail an exploration of this problem in Appendix A.

Our imaging setup instead makes use of two imaging modes: the first uses no mask, with a global $3\sigma_{\rm rms}$ threshold and up to five major iterations. $\sigma_{\rm rms}$ is calculated as a positionindependent value for each snapshot. This comparatively shallow CLEAN reduces the aforementioned bias, but results in up to $\approx 30\%$ higher rms noise in the output images. This is similar to the CLEAN threshold used for GLEAM and GLEAM-SGP, though we note some noise pixels may still be deconvolved in this case, depending on the observation. The second method retains the original masking and thresholding, but adds an additional mask. This additional mask restricts CLEAN to traditional boxes around sources from the sky model. The box size is set to 5 pixel \times 5 pixel. As this model is derived from deeper surveys than an individual snapshot image (namely GLEAM), almost all sources in a snapshot are included. We also restrict the mask further to sources that have > 25 mJy apparent flux density at 300 MHz, corresponding to approximately the lowest rms noise in any of the snapshots. We note that the automatic mask computed by WSClean is used within the regions covered by the sky model mask.

In general, the masking approach provides the best imaging quality and largely removes the aforementioned bias, however, around certain bright extended sources like Fornax A and in the Galactic Plane the masks are not adequate to capture the extent of the source so results in poorer images. For snapshots within Galactic latitudes of $|b| < 7.5^{\circ}$ and snapshots within 7.5° of specific bright extended sources $^{\rm p}$, we select the non-masked image, and select the masked image in all other cases where CLEAN did not diverge. We therefore use the masked image for 88% for the survey.

As in other GLEAM surveys, the snapshot data are split into four subbands during imaging by WSclean (-channels-out 4) to account for instrumental and physical spectral effects, with CLEAN components derived from the averaged full-band 30.72-MHz image. However, we do not retain the comparatively lower-sensitivity 7.68-MHz narrowband images. Sensitivity at 300 MHz is reduced compared to the lower part of the MWA band used for the rest of GLEAM (i.e. 72–231 MHz), and with more of the band flagged due to RFI—particularly below 300 MHz—the

lhttps://casa.nrao.edu/

^mThe default behaviour of the pipeline is to scale flux densities from 215 MHz reference values, so 77 Jy is scaled from 100 Jy at 215 MHz assuming a spectral index of -0.77, and 2.3 Jy is scaled from 3 Jy.

nhttps://gitlab.com/Sunmish/potato.

ohttps://gitlab.com/aroffringa/wsclean/.

^pOrion A, Taurus A, Fornax A, Centaurus A, and the radio galaxy associated with IC 4296, though note some of these overlap with the Galactic Plane selection.

narrow band images are significantly poorer quality than the equivalent images from the other GLEAM datasets.

2.3 Patching gaps with grating lobes

The lowest declination strip is at -72° and the mainlobe fullwidth at half-maximum (FWHM) is only $\approx 15^{\circ}$ so does not cover the South Celestial Pole (SCP). While there are no pointings towards the SCP, most of the observations in the declination -26.7° and -19.9° strips have significant primary beam grating lobes that provide coverage below $\delta_{J2000} < -72^{\circ}$, including the SCP, with maximum sensitivity at $\delta_{J2000} \approx -86^{\circ}$ and $\approx -76^{\circ}$, respectively. Figure 1(i) shows an example pointing with a grating lobe with a peak in sensitivity at $\delta_{12000} \approx$ -86° , covering the SCP. To ensure complete coverage of the Southern Sky we image these lobes for all the relevant observations, using the same calibration solutions for the given snapshot observation. We also repeat the peeling process, assuming the grating lobe is the pointing centre (as opposed to the main lobe) and continue with imaging and post-processing in an otherwise identical fashion.

In addition to the grating lobes covering the SCP region, we also use the equivalent grating lobes at $\delta_{J2000} \approx +32^{\circ}$ and $\approx +23^{\circ}$ from the declination -26.7° and -33.5° strips to provide survey coverage up to $\approx +40^{\circ}$. We refer to these additional data as separate declination strips in Table 1.

2.4 Post-imaging corrections

2.4.1 Primary beam and astrometry

After imaging we correct for the direction-dependent sensitivity pattern by applying the Full Embedded Element (FEE) model of the primary beam (Sokolowski et al., 2017). The images are clipped where they are attenuated by > 90% (i.e. the apparent brightness is < 10%). After primary beam correction, we use the source-finder aegean q (Hancock et al., 2012, 2018) to create a source list for each snapshot, keeping sources with peak brightness above $5\sigma_{\rm rms}$, where $\sigma_{\rm rms}$ is the local rms noise in the snapshot as calculated by the Background And Noise Estimation (BANE) tool packaged with aegean (Hancock et al., 2018). The source lists for each snapshot are cross-matched to the sky model used for initial calibration, and we use these cross-matched source lists to correct for position-dependent astrometric offsets using fits_warp.py (Hurley-Walker & Hancock, 2018). This process uses a position-dependent set of interpolated pixel shifts to align the image data with the global sky model.

2.4.2 The point-spread function

After imaging and source-finding with aegean, we inspect the ratio of integrated and peak flux densities ($S_{\rm int}/S_{\rm peak}$), comparing the median for each snapshot and each declination strip to check that the point-spread function (PSF) is appropriately estimated for each snapshot. To avoid extended sources, we construct a reference point source catalogue by combining the

Sydney University Molonglo Sky Survey (SUMSS; Bock et al., 1999; Mauch et al., 2003, at 843 MHz, $\approx 45 \times 45 \, \mathrm{arcsec^2}$ angular resolution), Molonglo Galactic Plane Survey (MGPS-2; Murphy et al., 2007), and the Rapid ASKAP ^s Continuum Survey (RACS; McConnell et al., 2020) 888-MHz catalogue (RACS-low; Hale et al., 2021, at 25×25 arcsec² angular resolution). We use SUMSS/MGPS-2 for the sky south of $\delta_{12000} < -80^{\circ}$ and RACS-low elsewhere. For RACS-low sources, we use the unresolved definition from Hale et al. (2021, see their section 5.2.1), and for SUMSS/MGPS-2 we consider a source unresolved if $S_{\rm int}/S_{\rm peak} < 1.2$. We also remove sources in the SUMSS/MGPS-2 and RACS-low catalogues that have neighbours within 4 and 3 arcmin, respectively. We crossmatch this unresolved and isolated RACS-SUMSS/MGPS-2 catalogue to the GLEAM-300 snapshot source list to identify point sources, but we do not enforce any similar selection criteria on the GLEAM-300 data.

Figure 3(i) shows the declination -55.0° signal-to-noise (SNR) weighted mean $S_{\rm int}/S_{\rm peak}$ ratios for cross-matched unresolved sources as a function of ObsID. In general, this ratio should tend towards > 1 (= 1 for an ideal point source), where residual extended sources and ionospheric blurring push the ratio above 1. With median ratios < 1 there are likely calibration, deconvolution, and/or a mismatched PSF issues. We find that for most snapshots this ratio is less than 1. The declination -55.0° strip has a median across all sources/snapshots of $0.91^{+0.05}_{-0.06}$, which reduces to $0.88^{+0.03}_{-0.05}$ for sources with peak flux densities above $100\sigma_{\rm rms}.$ The median across all declination strips is $0.96^{+0.07}_{-0.06}$ (reducing to $0.90^{+0.08}_{-0.05}$ for $100\sigma_{\rm rms}$ sources). For comparison, the equivalent GLEAM cross-match to the unresolved RACS-SUMSS/MGPS-2 catalogue has a median of $0.99^{+0.02}_{-0.03}$ at 200 MHz (with $0.96^{+0.11}_{-0.06}$ above $100\sigma_{\rm rms}$). The median ratios < 1 are likely related to calibration errors in this case due to mismatch between sky model and true sky (i.e. point sources being treated as extended or vice versa).

We attempt to correct for this by scaling the PSF (as the image restoring beam) which will leave the surface brightness in the images untouched, but allow for more accurate integrated flux density measurements. To avoid over-correcting individual snapshots, particularly those with a small number of sources, we opt to fit generic polynomial models to contiguous groups of ObsIDs for each night and for each declination strip separately. The groups are defined by ObsIDs that are not separated by more than 60 mins, and where the logarithmic ratios do not change by more than 0.05 to avoid jumps that require highorder polynomial models. This effectively creates a piece-wise polynomial model over the night. For fitting, we also use a sliding window filter across 10 ObsIDs and remove those with ratios greater than three times the standard deviation of the window. We also remove snapshots from fitting if they had less than 100 sources in the original source lists prior to cross-matching. For each group with a number of snapshots $N_{\rm obs} \ge 10$, we trial polynomial models up to degree $\lceil N_{\rm obs}/3 \rceil$, using the Bayesian Information Criterion (Schwarz, 1978) to select the model from the range of fitted models. Snapshots that

^qhttps://github.com/PaulHancock/Aegean.

rhttps://github.com/nhurleywalker/fits_warp.

^sAustralian SKA Pathfinder (Hotan et al., 2021).

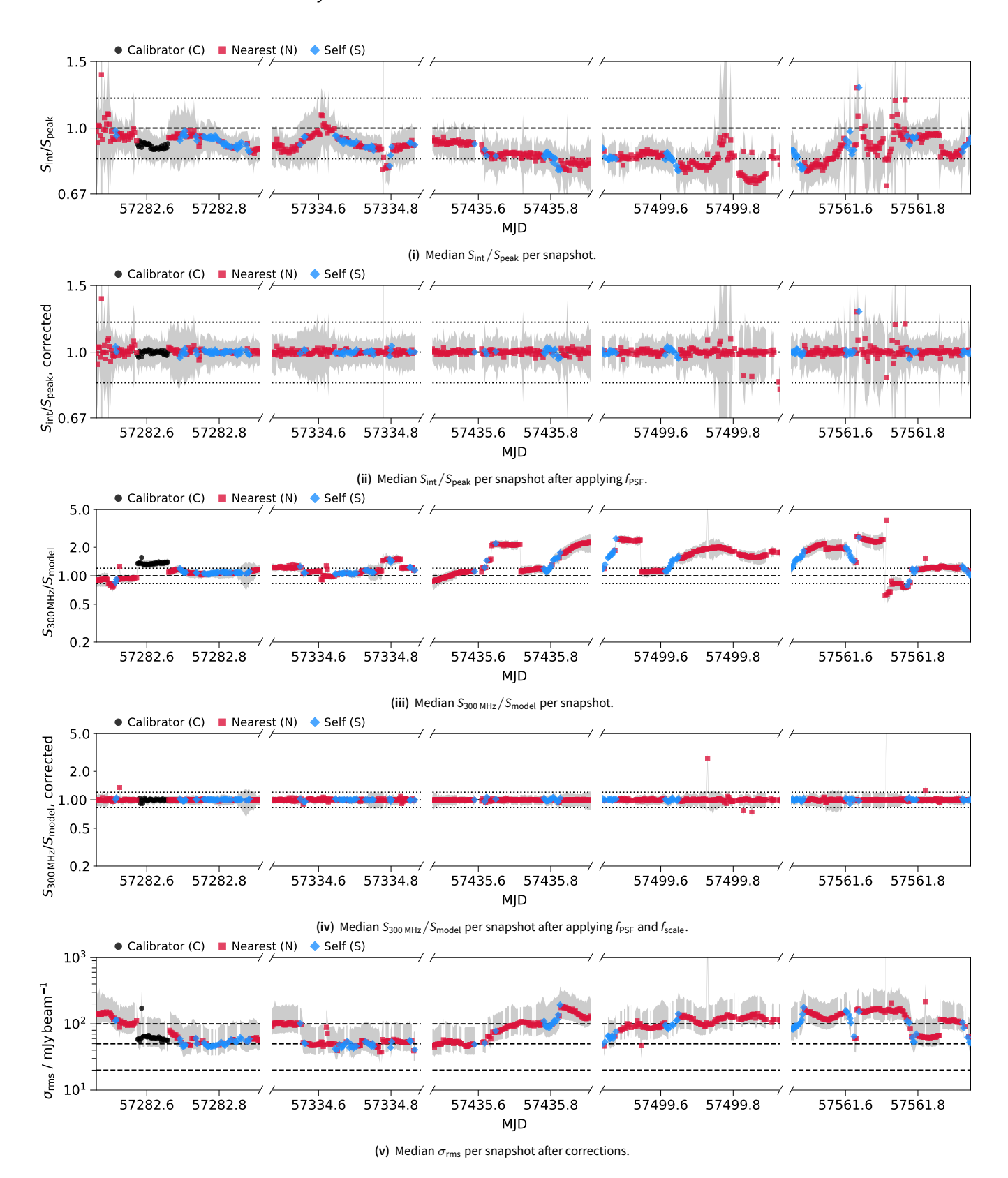


Figure 3. Basic image properties per snapshot for declination strip -55.0° . (i)–(ii) SNR-weighted mean $S_{\rm int}/S_{\rm peak}$ per snapshot after applying $f_{\rm PSF}$. The dashed horizontal line is drawn at 1, and the dotted horizontal lines are drawn at a ratio difference of 20%. (iii)–(iv) SNR-weighted mean flux density ratios, $S_{300\,\rm MHz}/S_{\rm model}$, comparing to the GGSM measurement, before and after applying $f_{\rm PSF}$ and $f_{\rm scale}$. The horizontal lines are as in (i). (v) median rms noise ($\sigma_{\rm rms}$) per snapshot after applying the brightness scale correction factor. Dashed horizontal lines indicate 20, 50, and 100 mJy beam⁻¹. In (i)–(iv), the grey shaded region is drawn between $\pm 1\sigma$ and in (v) between the 16-th and 84-th percentiles. Snapshots are coloured by their calibration solutions. Black circles: solutions derived from a dedicated calibrator scan; red squares: nearest-in-time best solutions from other observations; blue diamonds: solutions derived from the observation itself. Note for this declination strip, only a small number of snapshots used the dedicated calibrator solutions in the first night of observing. Note the y-axis in all panels is logarithmically scaled.

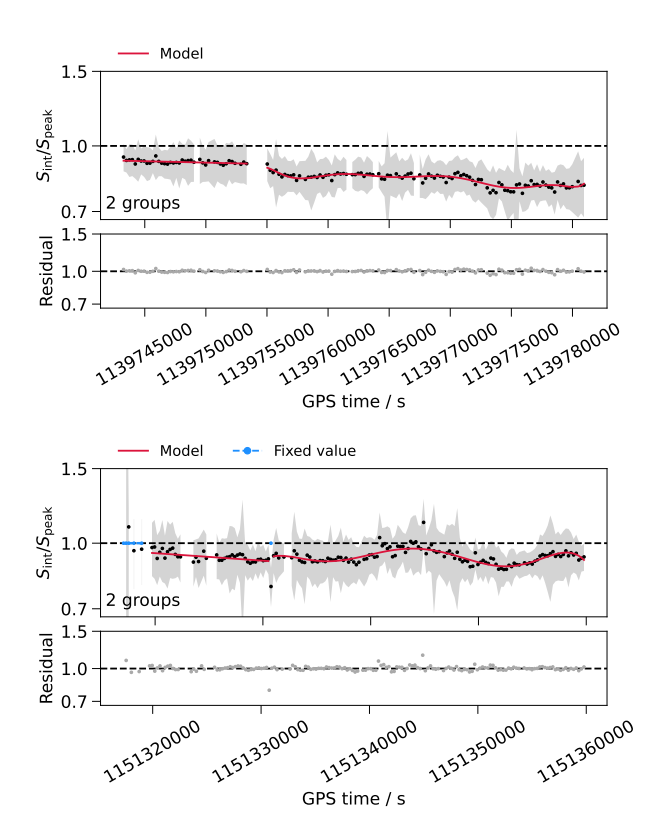


Figure 4. SNR-weighted mean $S_{\rm int}/S_{\rm peak}$ of sources cross-matched to the 'unresolved' RACS-SUMSS/MGPS-2 catalogue as a function of time for two example nights ($top\ panels$) and the residual ratio ($bottom\ panels$). The black points indicate SNR-weighted mean values for a given ObsID, and the red solid lines indicate fitted polynomial models to each group as described in the text and the blue dashed lines with blue markers indicate a fixed value was assigned (only relevant for the bottom panel in this case). The gray shaded regions show $\pm 1\sigma$ for each snapshot. The residuals after applying the model values are shown in the bottom panels.

do not lie within a fitted group will take the median value for the night, or a value of 1 if no groups were fit for that particular night, and those within the group range will take a fitted value from the selected model. These PSF correction factors, $f_{\rm PSF}$, are applied to the FWHM of both the PSF major and minor axes as $\theta_{\rm corrected} = \theta \sqrt{f_{\rm PSF}}$. Figure 4 shows two example nights of $S_{\rm int}/S_{\rm peak}$ highlighting the results of the piece-wise polynomial fitting.

Due to the lack of coverage of the RACS-SUMSS/MGPS-2 catalogue, we also cross-match the $\delta_{\rm J2000}=+32.0^\circ$ grating lobe strip to the NVSS and check the results against the $\delta_{\rm J2000}=-26.7^\circ$ mainlobe strip. We find similar ratios of $S_{\rm int}/S_{\rm peak}$ within the standard deviation for the ObsIDs, but with more significant scatter. For this reason, we assume the $\delta_{\rm J2000}=+32.0^\circ$ grating lobe declination strip mirrors the main lobe in terms of the resultant PSF correction and use the corrections derived from the mainlobe images. After application, the median ratio for unresolved sources across all snapshots is $1.02^{+0.04}_{-0.03}$ ($0.98^{+0.02}_{-0.02}$ for $100\sigma_{\rm rms}$ sources), bringing the 300 MHz data closer to the expected ratio of 1.

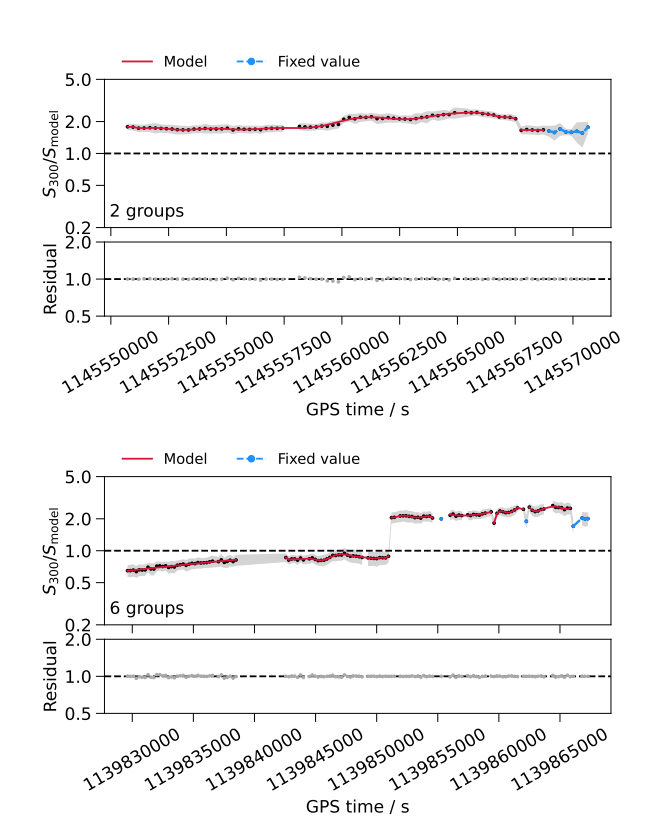


Figure 5. Models of the per-ObsID brightness scale correction factors for two example nights (*top panels*) and the residual ratio (*bottom panels*). The black points indicate weighted mean values for a given ObsID, and the red solid lines indicate fitted polynomial models to each group as described in the text. The shaded, gray regions show the weighted standard deviation. The blue dashed lines with blue markers indicate a fixed value was assigned based on the weighted mean of the individual ObsID.

2.4.3 Snapshot brightness scale

After application of the primary beam model, we also compare the measured flux densities of sources in the 300 MHz images compared to the sky model to check the overall brightness scale of the snapshot images. To compare, we cross-match sources detected above $10\sigma_{\rm rms}$ and with $S_{\rm int}/S_{\rm peak} < 1.2$ in the 300-MHz snapshots to the sky model and scale the sky model flux densities to 300 MHz using the reported spectral indices. This is done after application of the PSF correction factors. We noticed residual variation to the brightness scale as a function of ObsID. Figure 3(iii) shows the SNR-weighted mean measured to model flux density ratio $(S_{300 \text{ MHz}}/S_{\text{model}})$ per ObsID as a function of time for the declination -55.0° strip. We also see variation as a function of time/ObsID for all declination strips, with some link to specific calibration solutions (i.e. the ratio between observations that share a set of solutions shows less variation generally). While not shown in the SNR-weighted mean values, we also see no significant variation in brightness scale as function of position across the images, but the residual variation as a function of ObsID is likely related to variation in the local sky model for each ObsID and how nearest-in-time 'good' solutions are applied to observations.

To correct this residual brightness scale variation, we perform a similar polynomial fitting procedure for the ratio

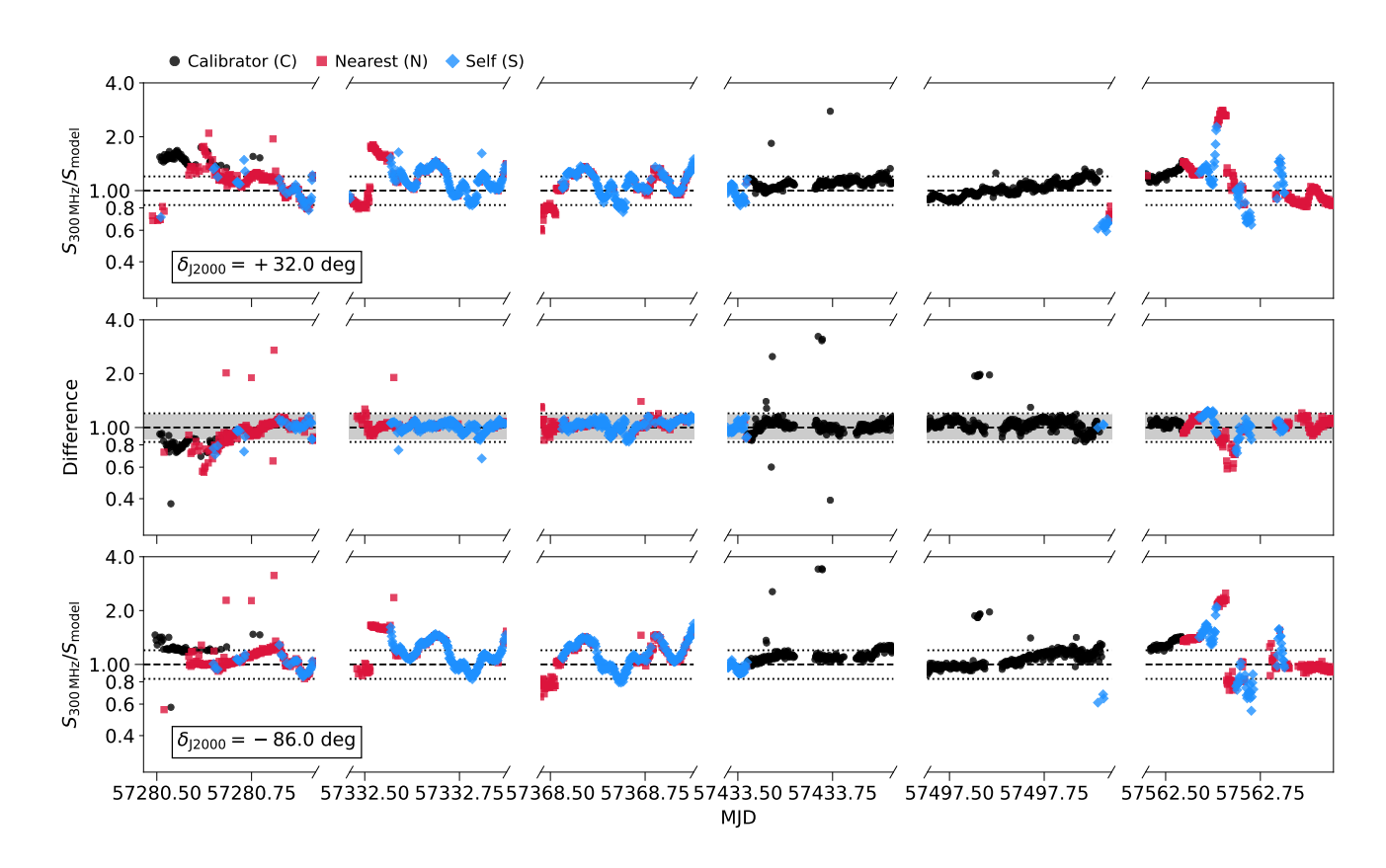


Figure 6. SNR-weighted mean flux density ratios, $S_{300\,\mathrm{MHz}}/S_{\mathrm{model}}$, comparing to the extrapolated sky model measurement for grating lobe images that make up the δ_{J2000} = +32.0° (top panel) and -86.0° (bottom panel) declination strips. The middle panel shows the difference in the SNR-weighted mean ratios between the two strips for each ObsID. The shaded region in the middle panel is drawn at $\pm 1\sigma$ (16%), and the dashed and dotted lines in each panel are drawn at a ratio of 1 and $\pm 20\%$, respectively. The points are coloured by their calibration solutions type, as in Figure 3. The y-axis scale is logarithmic, though has a reduced range compared to the flux density ratios on Figure 3.

 $S_{300\,\mathrm{MHz}}/S_{\mathrm{model}}$, using the SNR-weighted mean ratio per snapshot, with model-fitting weights determined by the sum of weights from flux density measurement uncertainties at 300 MHz. We restrict the ratios to 0.1–10, with a slightly larger logarithmic jump of 0.1 to determine where fitting group boundaries are defined. After obtaining the models, we apply the brightness scale correction factor, f_{scale} , to snapshots by evaluating the models for snapshots within a group that was fit. For snapshots that were not part of a fitted group, we take the measured SNR-weighted mean ratio as f_{scale} if over 25 sources were in the cross-match, otherwise snapshots not in a group and with few cross-matches are discarded. Figure 5 shows the SNR-weighted mean flux density ratios along with the fitted models for two example nights from the declination -72.0° strip (top panel) the declination -19.9° strip (bottom panel), highlighting the general shape and variance of the polynomial models.

The GLEAM flux density scale uncertainty is reported to be 80% for $\delta_{J2000} < -83.5^{\circ}$ and our sky model makes use of NVSS-VLSSr sources above $\delta_{J2000} \gtrsim +30^{\circ}$ so it is important to check the validity of the brightness scaling process for the grating lobe images in those regions. We compare the flux density ratios calculated for the $\delta_{J2000} - 86.0^{\circ}$ and $+32.0^{\circ}$ images, which are derived from the same observations and

calibration solutions.

Figure 6 shows the flux density ratios of the ObsIDs with the sky model in the far grating lobe images (top panel δ_{J2000} = $+32.0^{\circ}$ and bottom panel $\delta_{\rm J2000} = -86.0^{\circ}$) along with the difference in the ratios for each ObsID (middle panel). The general form of the flux density ratios is similar between the two declination strips except around complex regions (e.g. ObsIDs where the main lobe covers the Galactic Centre), but with some residual small-scale features. The standard deviation of the difference between the ObsIDs is $\approx 16\%$, which we take as an intrinsic brightness scale error for these regions (see Section 4.6.2 for details on the final brightness scale uncertainty). This reduces to $\approx 6\%$ after application of f_{PSF} and f_{scale} . We note that comparisons of the far grating lobe data with the main lobe data for those ObsIDs returns almost identical standard deviations, though with an additional time-independent offset likely related to the primary beam models which is implicitly corrected for in this post-image scaling

3. Stacked images

3.1 Mosaics

After post-imaging corrections, snapshots are combined via linear mosaicking to form full-sensitivity images at 300 MHz. Because of the smaller FoV at 300 MHz, observations typi-

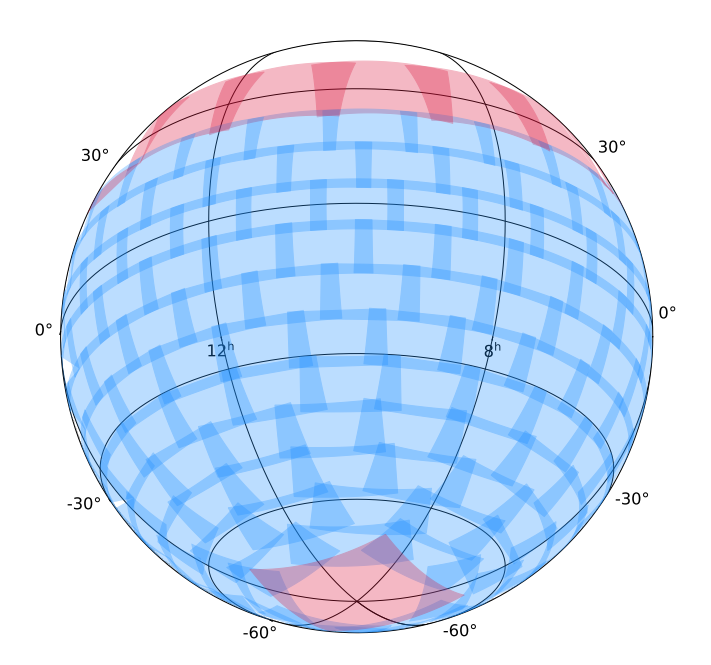


Figure 7. Mosaic and source-finding regions in orthographic projection. The grating lobe regions are shown in red (SCP cap region and high-declination regions). Only regions on the front side of the sphere are shown.

cally have less overlap compared to the GLEAM/GLEAM-X observations in the lower part of the MWA band even with the additional declination strips. A smaller FoV allows us to mosaic smaller regions than the full declination strip mosaics used for GLEAM, though there is still some redundancy in the mosaic processing. Therefore, we follow a similar mosaicking process used for the RACS-low (Hale et al., 2021) to create full-sensitivity images in regions covering

$$f_{\rm pad}[15^{\circ} \times 9^{\circ}]. \tag{1}$$

The regions are placed with equal spacing between $-72^{\circ} \le \delta_{\rm J2000} \le +18^{\circ}$, with dimensions in $\alpha_{\rm J2000}$ scaled by $\cos \delta_{\rm J2000}$. These regions are shown in blue on Figure 7. We include a padding factor, $f_{\rm pad}=1.2$, in the region size to ensure overlap between the regions so that extended sources are less likely to be cut off during source-finding.

We include additional regions covering the SCP and high-declination grating lobe images (highlighted red in Figure 7). The SCP mosaic is $30\times30\,\mathrm{deg^2}$ and the large high-declination mosaic regions are centered on $\delta_{\mathrm{J2000}}=+32.0^\circ$, with dimensions of $26.3\times19.2\,\mathrm{deg^2}$, following a similar padding and spacing as the main lobe regions.

There are a total of 217 mosaic regions, covering $-90^{\circ} \le \delta_{\rm J2000} \lesssim +40^{\circ}$. These regions are formed from the linear mosaic of all snapshots with image centres within 5 degrees of region boundary or with centres within the region boundary. Due to the generally lower quality of the grating lobe images, we only use the grating lobe images in the specific grating lobe regions. This results in 87–461 snapshots per non-SCP region, and 2 046 for the SCP region (which draws also from the $\delta_{\rm J2000} = -72.0^{\circ}$ snapshots). We use a position-dependent rms map as weights to stack the snapshots via a weighted average.

The rms map is generated by BANE, where we increase the grid and box size (100 and 500 pixels) used for calculating the rms to ensure a smoothly varying rms estimate that largely follows the primary beam sensitivity.

Prior to forming the individual mosaics, we also convolve all snapshots within a mosaic group to the lowest common angular resolution of that particular group. We make use of the convolution tools from RACS-tools t which makes use of the common_beam function from the radio-beam Python package u to find the smallest PSF that the group can be deconvolved by, ensuring all snapshots can be convolved to a matching resolution. To ensure that the resolution does not become too degraded, we remove snapshots that have a PSF major axis (θ_{major}) that is $> \overline{\theta_{\text{major}}} + 2\sigma_{\theta_{\text{major}}}$ where $\overline{\theta_{\text{major}}}$ is the mean PSF major axis of the snapshot group and $\sigma_{\theta_{\text{major}}}$ is the standard deviation. For the SCP, we restrict this further to a $0.5\sigma_{\theta_{major}}$ variation to avoid an overly-large PSF in some of the SCP images and because there is a significant amount of overlap in images for this region. In addition to removal of snapshots with large PSFs, we also filter snapshots based on the median root-mean-square noise and we remove 99 snapshots where the Moon was present within the image boundaries.

Figure 8 shows the example mosaic containing the bright radio galaxy Fornax A. That particular mosaic presents a 'best-case' for imaging quality as Fornax A provides a strong model for in-field calibration and most snapshot images in this region arrive at good solutions. The median rms noise for the mosaic in Figure 8 is $5.6^{+0.8}_{-0.6}$ mJy beam⁻¹. Figure 9 highlights the imaging quality in the Galactic Plane, showing a mosaic covering the plane and Galactic longitudes of $285^{\circ} \lesssim l \lesssim 308^{\circ}$. The median noise in this region is higher than the Fornax A example, at $14.1^{+10.9}_{-3.1}$ mJy beam⁻¹, owing to the number of complex and bright extended sources that are not as well-modelled or well-calibrated as Fornax A.

A region with low rms noise at high-declination is shown in Figure 10—a median rms noise of $16.5^{+3.7}_{-2.7}$ mJy beam $^{-1}$ is a best-case scenario for the most northern part of the survey. High-declination mosaics are constructed from low-elevation pointings and grating lobes which have lower sensitivity. Finally, Figure 11 shows the full mosaic covering the SCP. Due to the significant overlap in images here the median rms noise is $12.2^{+4.0}_{-1.9}$ mJy beam $^{-1}$. This region features noticeable ripples radiating from the SCP, likely residual RFI in the declination -26.7° scans. The same ripples can be seen in the mainlobe images, though at a much lower level. In addition, all of the grating lobe regions (SCP and high-declination) tend to feature more significant large-scale background undulations than elsewhere.

3.2 Source finding and source lists

Once mosaics are made, we use aegean to generate lists of 2-D Gaussian components. We use BANE again to create a position-dependent rms noise and background map for each mosaic, used by aegean for source-finding thresholds and

thttps://github.com/AlecThomson/RACS-tools.

uhttps://github.com/radio-astro-tools/radio-beam.

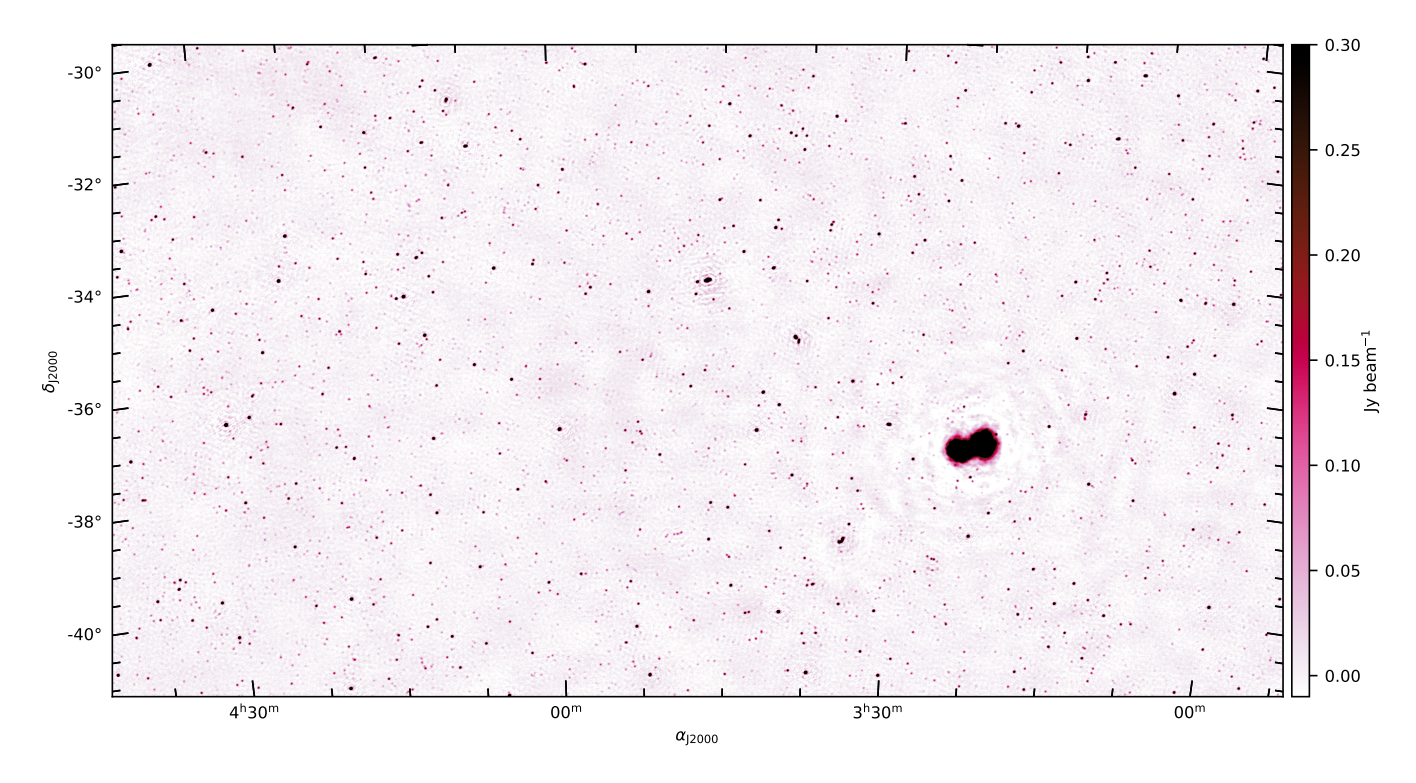


Figure 8. Example mosaic covering $21.0^{\circ} \times 11.7^{\circ}$ containing the radio galaxy Fornax A. The image represents the region of sky close to lowest rms noise $(5.6^{+0.8}_{-0.6} \text{ mJy beam}^{-1})$ in the survey, partly due to the strong and well-modelled in-field calibrator.

measurements. For the mosaics, we use a $4\sigma_{rms}$ threshold for source detection (the 'seedclip' parameter in aegean), and $3\sigma_{rms}$ for growing source detections ('floodclip'). This process is consistent with source-finding from other GLEAM data releases, focusing on compact sources. While our initial source-finding threshold is $4\sigma_{rms}$ we remove any components with a peak flux density $<5\sigma_{rms}$ from each source list. In addition, we remove sources with reported integrated flux density uncertainties greater than 100% of the measured value, with $\approx 1\text{--}20$ sources removed from a median $\approx 2\,500$ sources per mosaic. For example, the mosaic region with Fornax A in Figure 8 contains 3 861 components above $5\sigma_{rms}$.

3.3 Completeness

Due to difference in image properties, we investigate how complete the source lists for each mosaic region are expected to be prior to combining them into a single catalogue. We follow the process used for other GLEAM data releases (Hurley-Walker et al., 2017, but see also Franzen et al. 2021; Hurley-Walker et al. 2022a; Ross et al. 2024). We inject point sources onto our images using AeRes (Hancock et al., 2012, 2018) with pseudo-random positions (requiring no neighbours within 4 arcmin) and for multiple realisations at a range of logarithmically-spaced flux densities from 0.012–1 Jy. The number of sources varies per mosaic region, corresponding to ≈ 10 sources per square degree matching the overall source density in the final catalogue (Section 4). The completeness is defined by the number of injected sources that are recovered at each injected flux density level after repeating the same source-finding process

used for the normal images. We note that this method largely assesses the source-finding approach and does not take into account how other instrumental effects such as (u,v) coverage would affect recovery of sources.

The median flux density limit at 50% completeness is 45^{+12}_{-16} mJy (ranging from 21–141 mJy) and at 95% is 89^{+89}_{-33} (ranging from 45–891 mJy) across the mosaic regions. We show the 50% and 95% complete flux density limits as a function of position in Figure 12. The data are shown as a average for each tile, with nearest-neighbour interpolation to generate a contiguous map. Generally, completeness decreases in the Galactic Plane where large, extended Galactic radio emission is present, and around areas with significant artefacts following positional variation of the rms noise across the survey (see Section 4.3). Completeness metrics are included in the FITS headers for each mosaic image.

4. The 300-MHz catalogue

4.1 Merging source lists

The mosaic regions have a significant overlap by construction so any combined source catalogue needs to have duplicate measurements from sources detected across adjacent mosaics removed. We follow the method of Duchesne et al. (2024) and construct the full catalogue by concatenating the source lists one-by-one. As each source list is added, we cross-match the incoming source list to the partially constructed catalogue with a separation of $0.5 \times \langle \Theta_{\text{major}} \rangle$, where Θ_{major} is the fitted major axis FWHM of the Gaussian component. Any sources cross matched within half their averaged size are considered

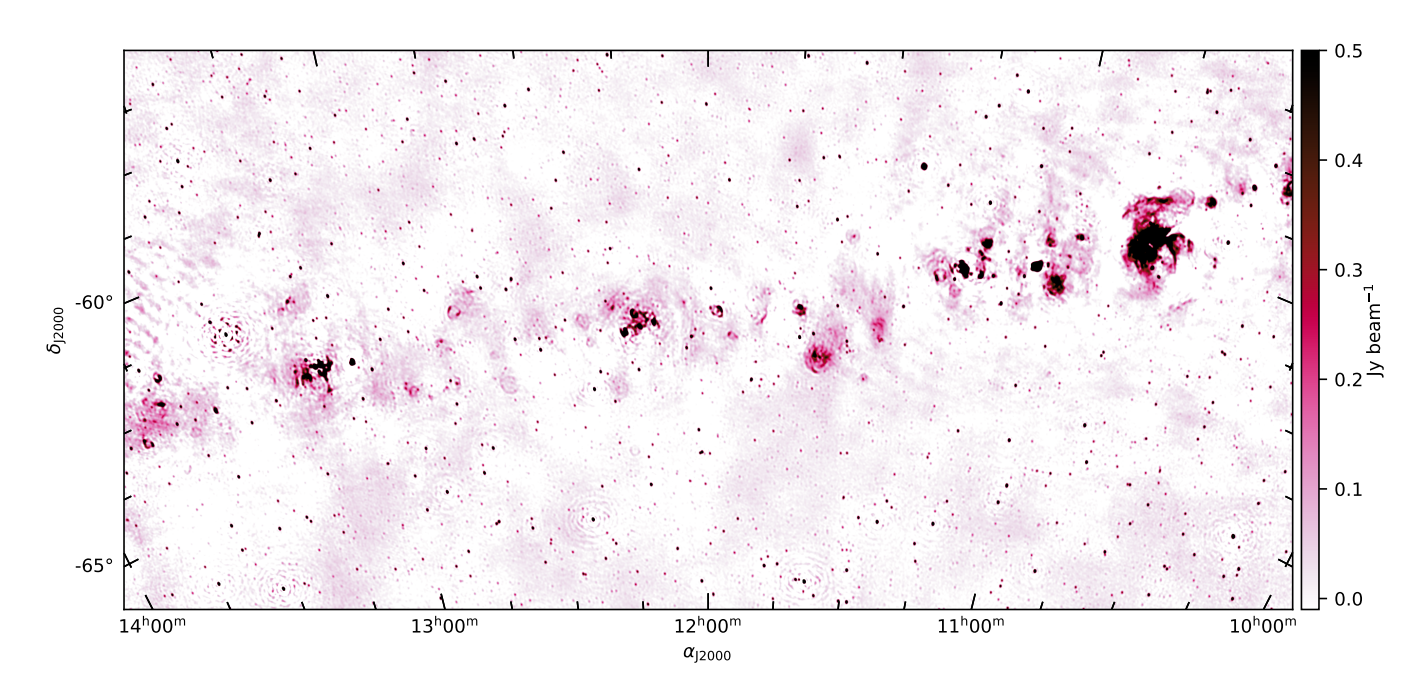


Figure 9. Example mosaic covering $24.5^{\circ} \times 11.7^{\circ}$ covering Galactic longitudes $285^{\circ} \lesssim l \lesssim 308^{\circ}$, showing the background ripples due to the extended sources. The median rms noise of the mosaic is $14.1^{+10.9}_{-3.1}$ mJy beam $^{-1}$.

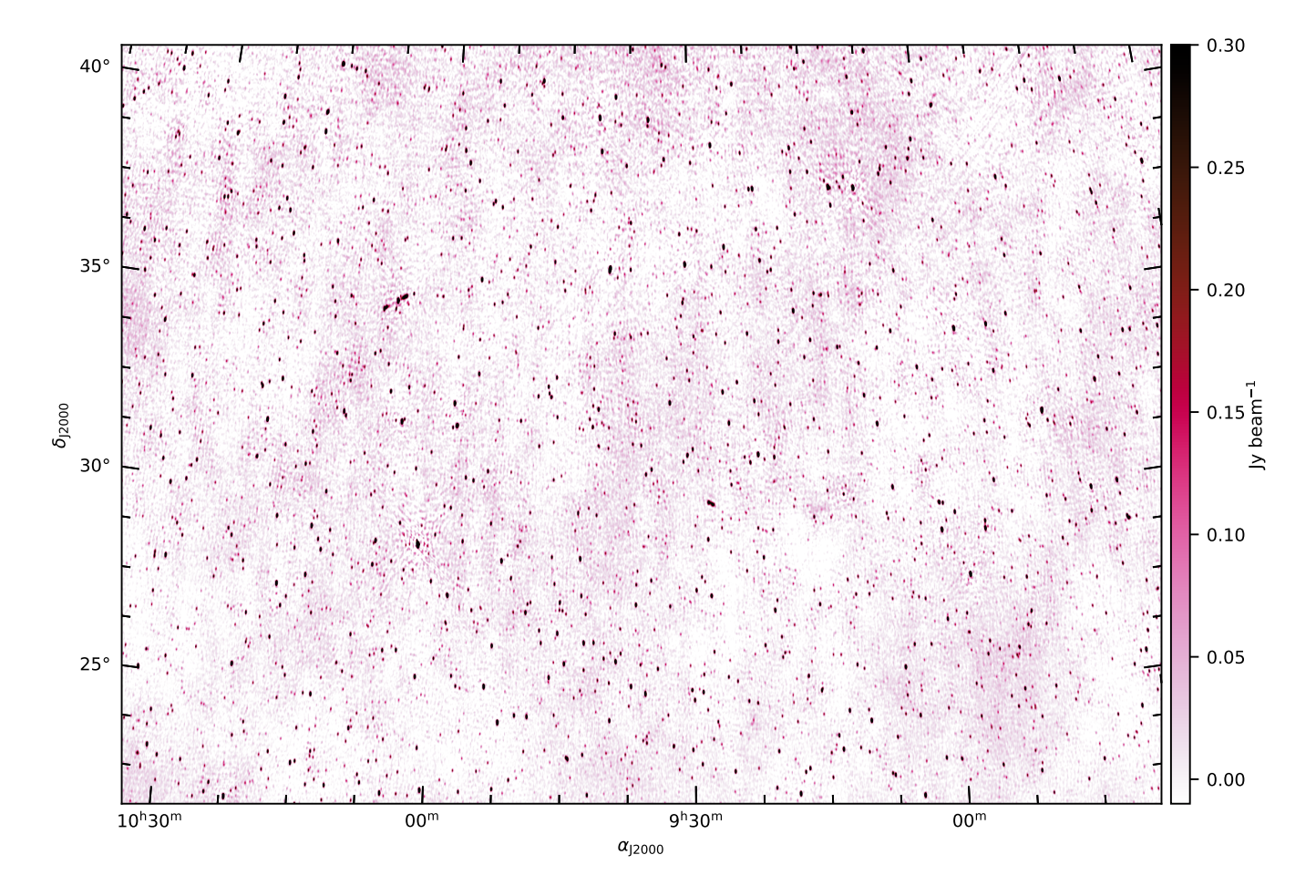


Figure 10. Example mosaic at high declination covering $26.3^{\circ} \times 19.2^{\circ}$, representing the lowest noise $(16.5^{+3.7}_{-2.7} \, \text{mJy beam}^{-1})$ for the northern part of the survey.

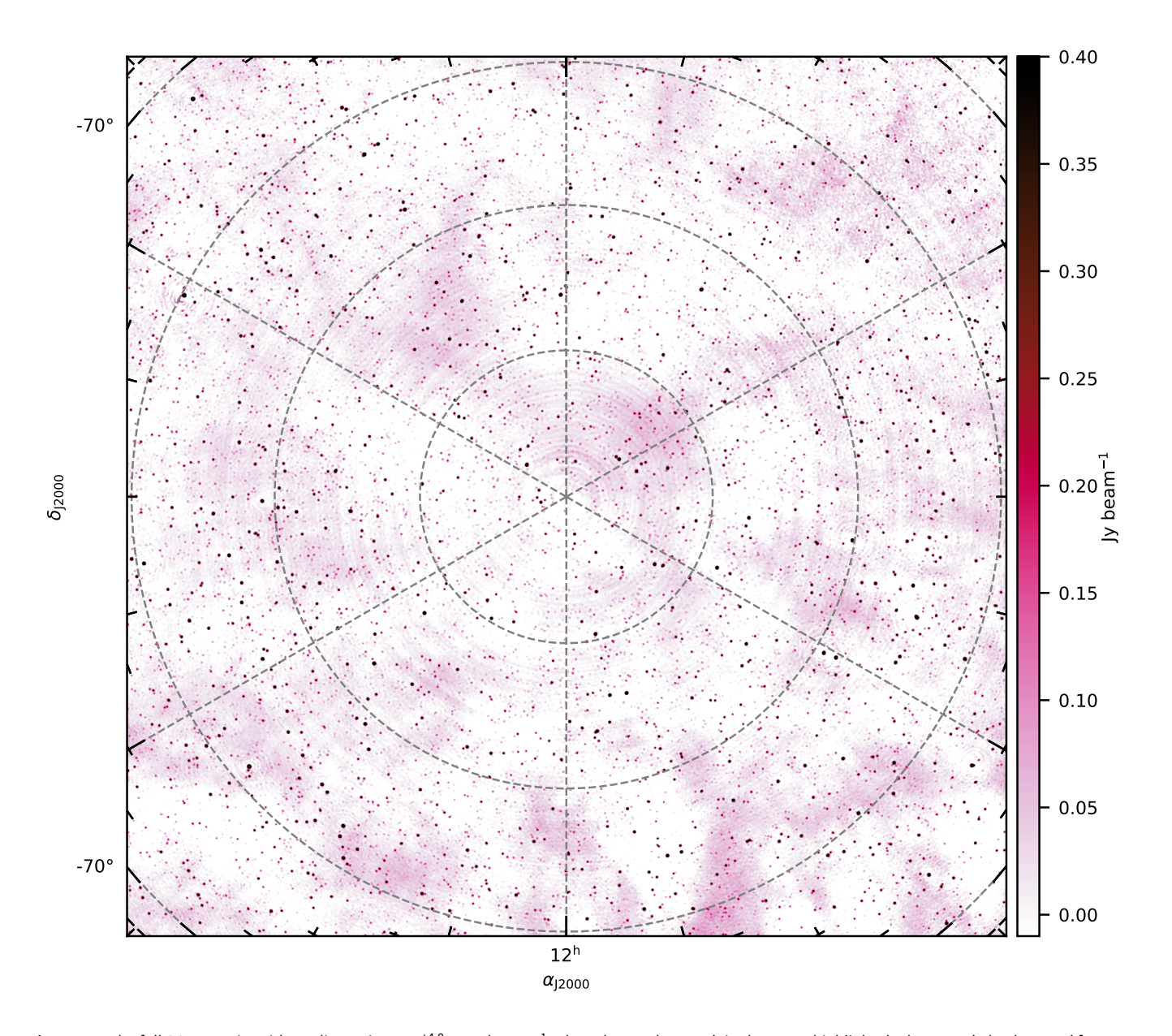


Figure 11. The full SCP mosaic, with median noise $12.2^{+4.0}_{-1.9}$ mJy beam $^{-1}$. The colourscale stretch is chosen to highlight the large-scale background features.

duplicate measurements of the same source. For duplicated measurements, we opt to keep the measurement from the mosaic lowest rms noise at the location of the source. The resultant merged catalogue contains 338 080 components, with a median density of $\approx 10\, deg^{-2}$. Figure 13 shows the component density across the whole survey using HEALPix $^{\rm v}$ binning, generally highlighting regions of lower/higher sensitivity (see Section 4.3).

4.2 Catalogue columns

The information included in the catalogue is similar to a single frequency from GLEAM-X, with component coordinates, measured sizes and flux densities, and additional metadata useful for further measurements or comparisons to other catalogues. The columns are summarised as:

- 1. name: Component name following IAU convention: GLEAM-300 JHHMMSS±DDMMSS.
- RAJ2000: J2000 right ascension of the component in decimal degrees.
- 3. err_RAJ2000: Uncertainty on right ascension from fitting the component position in decimal degrees.
- 4. DEJ2000: J2000 declination of the component in decimal degrees.
- 5. err_DEJ2000: Uncertainty in declination from fitting the component position in decimal degrees.
- 6. local_rms: Estimate of the local root-mean-square noise in Jy beam⁻¹.
- 7. background: Estimate of the local background in

^vHierarchical Equal Area isoLatitude Pixelation (Górski et al., 2005).

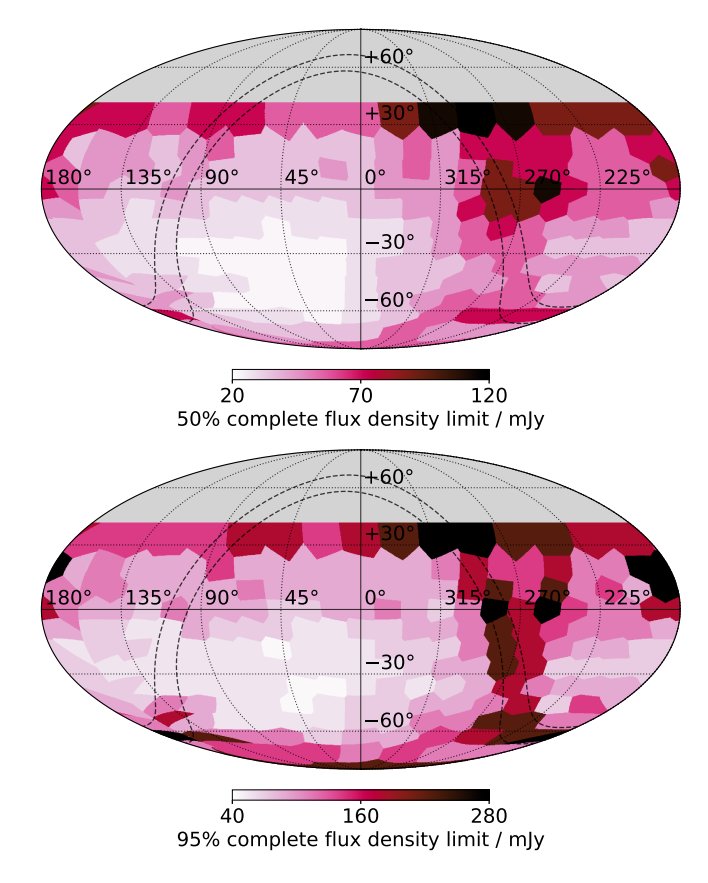


Figure 12. 50% (*top*) and 95% (*bottom*) flux density completeness limits across the survey. The limits are represented by an average over each mosaic region, with nearest-neighbour interpolation. Note each panel uses a different colourscale.

Jy beam $^{-1}$.

- 8. peak_flux: Peak flux density of the component in Jy beam $^{-1}$.
- 9. err_peak_flux: Uncertainty in the peak flux density in Jy beam⁻¹.
- int_flux: Integrated flux density of the component in Jy.
- 11. err_int_flux: Uncertainty in the integrated flux density of the component in Jy.
- 12. a: FWHM of the major axis of the component in arcsec.
- err_a: Uncertainty in the FWHM of the major axis in arcsec.
- 14. b: FWHM of the minor axis of the component in arcsec.
- err_b: Uncertainty in the FWHM of the minor axis in arcsec.
- 16. pa: Position angle of the component in degrees.
- 17. err_pa: Uncertainty in the position angle in degrees.
- 18. bma j: Local major axis of the beam in arcsec.
- 19. bmin: Local minor axis of the beam in arcsec.
- 20. bpa: Local position angle of the beam in degrees.
- 21. flags: Aegean fitting flags.
- 22. flux_scale_err: Declination-dependent brightness scale fractional uncertainty (Section 4.6.2).

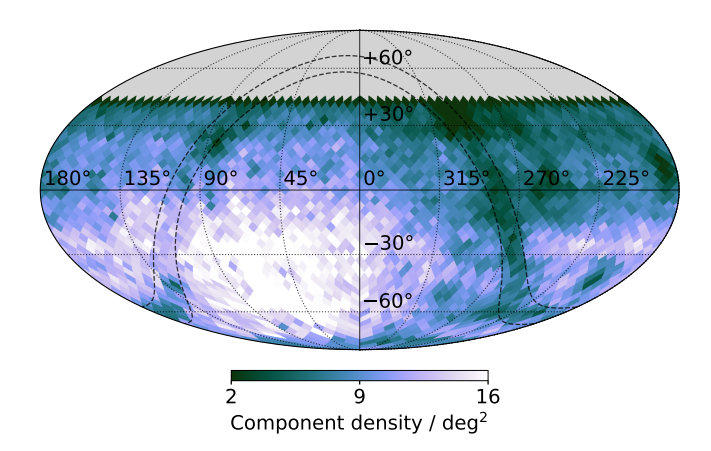


Figure 13. The density of Gaussian components across the survey in HEALPix bins of 13.4 \deg^2 .

4.3 Noise

The rms noise in the final mosaic images varies across the survey, with a median value of $9.1^{+5.5}_{-2.8}\,\mathrm{mJy\,beam^{-1}}$. Figure 14 shows the HEALPix-binned map of the rms noise as reported in the catalogue. The noise is raised around some bright sources and in regions of the Galactic Plane, with some additional increase in noise around $\alpha_{J2000}\approx270^\circ$ and $\delta_{J2000}\approx-13^\circ$ to $\approx+1.6^\circ$ due to calibration challenges in this region. Some of the high-declination mosaics feature higher noise due to complex bright sources within the images (Cygnus A) and within the main lobe (the Galactic Centre)—these are peeled/removed when outside of the FoV, but significant artefacts still remain in some cases. Figure 9 also shows typical large-scale background features present near the extended sources in the Galactic Plane.

4.4 Image artefacts

In common with most all-sky surveys, the 300-MHz images feature noticeable artefacts at the $\approx 1\%$ level, from both position-dependent and position-independent errors around bright sources. These artefacts can be mitigated with self-calibration, and are reduced when using in-field calibration, although with our processing strategy self-calibration is not done due to a high failure rate and in-field calibration is only done for a subset of the snapshots. Common artefacts following the general shape of the PSF around bright sources are shown in Figure 15, highlighting the form of the errors for $\delta_{J2000} \gtrsim 0^\circ$ (Virgo A, left) and for $\delta_{J2000} \ll 0^\circ$ (PKS 1932–46, right). Despite the lack of self-calibration, we are able to achieve a dynamic range of at least ≈ 90 with typical errors $\approx 1\%$.

4.5 Catalogue reliability

A common method of determining the number of false positive detections around bright sources (hence the reliability of the source finding) is to repeat source-finding on the same images multiplied by -1 (i.e. the 'negative' image, or 'inverted' image; e.g. Intema et al. 2017; Hale et al. 2021; Hurley-Walker et al. 2022a; Ross et al. 2024). Assuming the noise and artefacts are Gaussian and symmetric, a measure of source-finding

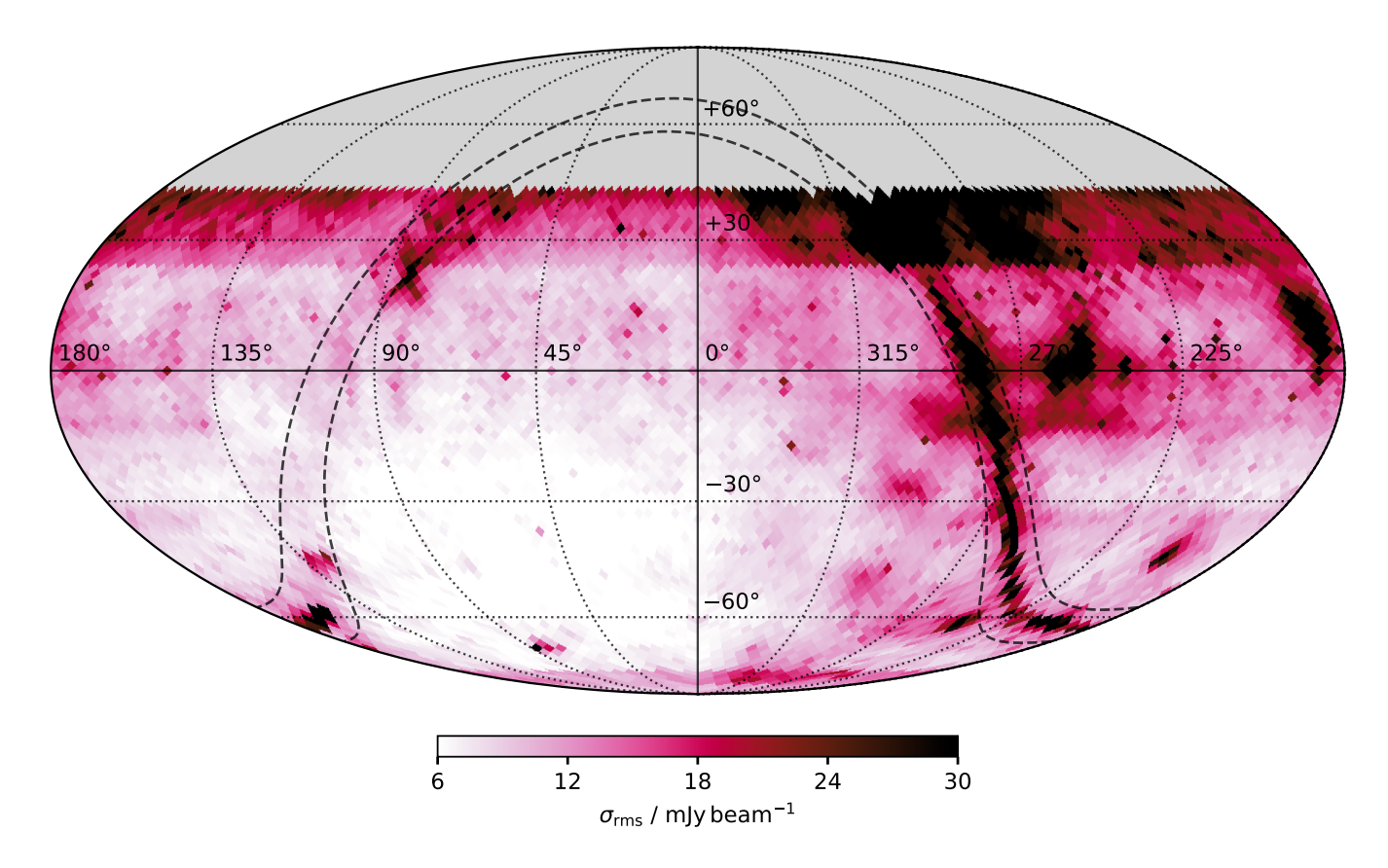


Figure 14. HEALPix representation of the local rms noise at the position of sources in the constructed catalogue.

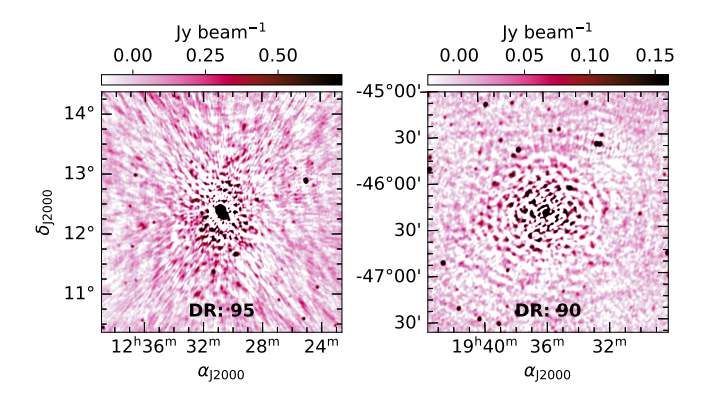


Figure 15. Common artefacts around bright sources for declination $\gtrsim 0^\circ$ (Virgo A, left) and declination $\ll 0^\circ$ (PKS 1932—46, right). The dynamic range (DR) is shown, estimated based on peak values of the sources and the most significant nearby artefacts.

reliability, r, is then defined as

$$r = 100 \times (1 - N_{\text{negative}}/N_{\text{positive}}) \%, \tag{2}$$

for $N_{\rm negative}$ sources found in the negative image and $N_{\rm positive}$ sources found in the original image.

To help reduce the number of artefacts that are included in the catalogue, we filter catalogued Gaussian components around bright ($S_{\text{bright}} = S_{300} > 1\,\text{Jy}$) sources. This process is modified from the artefact filtering done for GLEAM-X

DR1/DR2 (Hurley-Walker et al., 2022a) with the inclusion of a simplified flux-dependent radial filter (see e.g. Knowles et al., 2022, for a similar method). We do this prior to merging source lists. We define a beam- and flux-dependent filter around sources that scales linearly between $5-20 \times \theta_{\text{major}}$ for bright sources between $1-5 \,\mathrm{Jy}$. Sources with flux densities $> 5 \,\mathrm{Jy}$ use a fixed $20 \times \theta_{\text{major}}$ radius. All catalogued components within the defined radius of a bright source are considered artefacts if they are sufficiently fainter than the bright source by $S_{\text{faint}} \times 100 < S_{\text{bright}}$. In addition, if a 'negative' source lies within the filter radius, we reduce the filter radius to match the maximum angular separation between the bright source and any negative sources. We then consider any positive source within the same absolute flux limit as the negative source to also be an artefact. Negative sources satisfying these conditions are also removed from their respective source lists. An example 2.4-Jy source is shown in Figure 16, with sources within the $12.1 \times \theta_{\text{major}}$ radius shown, with markers indicating whether they are artefacts or not. The positive artefacts either side of the source are common source sidelobe artefacts seen in that region.

We perform the assessment of the reliability after removing artefacts on the final catalogue and negative catalogue. The overall reliability in the catalogue is 99.58%, and Figure 17 shows the reliability of all mosaics combined as a function of SNR ($S_{\rm peak}/\sigma_{\rm rms}$). Reliability generally increases with increasing SNR, with $\approx 99\%$ reliability achieved at $\approx 6.0\sigma_{\rm rms}$,

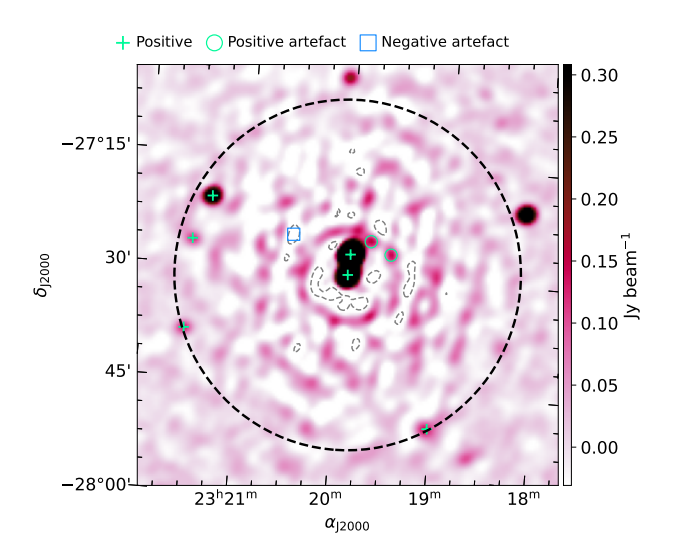


Figure 16. Example of the artefact filtering process. The panel is centered on a 2.4 Jy component. Positive and negative components within the initial filter radius are shown, with markers indicating whether they are considered artefacts or not (see legend). The single dashed-grey contour is drawn at $-3\sigma_{\rm rms}$.

and 100% reliability above $\approx 10\sigma_{rms}$. We note Franzen et al. (2021) reports an overall higher reliability for the GLEAM SGP catalogue, likely a result of self-calibration reducing artefacts around bright sources. We note that the SCP region has comparatively higher overall reliability at 99.94%, while the high-declination regions more closely match the main survey at 99.71%.

4.6 Photometry

4.6.1 The point spread function

As the individual mosaics have different angular resolutions, the PSF for sources in the catalogue also varies across the sky. Figure 18 shows the position-dependent major and minor axes of the image PSF as recorded in the catalogue using HEALPix binning. The median major and minor axes are 128."8 × 112."5, and range from 108."8–275."7 and 89."4–222."8, respectively. The PSF major and minor axes largely vary as a function of declination, with some additional variation around specific regions, relating to areas with either fewer snapshots, more RFI flagging, or poorer calibration. In particular, the high-declination and SCP regions feature the largest PSFs, corresponding to the lower elevation of the grating lobe directions.

Figure 19 shows the ratio of $S_{\rm int}/S_{\rm peak}$ as a function of source SNR for all sources in the catalogue. The overall median ratio is $0.99^{+0.19}_{-0.10}$, reducing slightly to $0.98^{+0.06}_{-0.02}$ for sources with SNR > 100, consistent with results from the individual snapshots prior to mosaicking (Section 2.4.2).

4.6.2 The brightness scale

The brightness scale is set by the input sky model we use for calibration and post-processing so we expect the final mosaics to be consistent with GLEAM and GLEAM-X by extension. To assess any residual brightness scale errors we com-

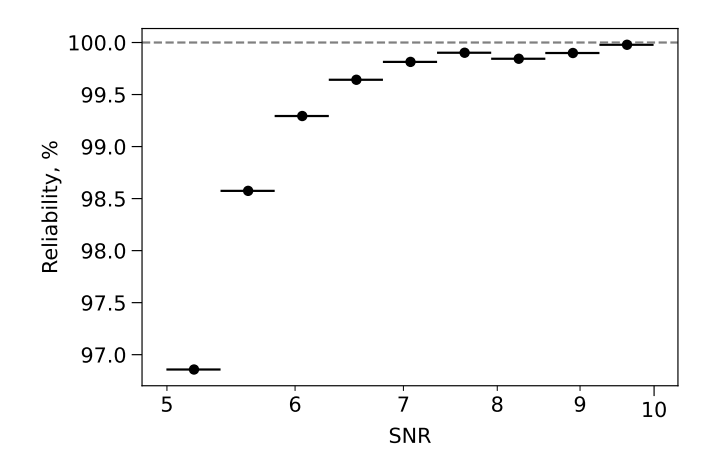


Figure 17. Reliability as a function of SNR. The dashed horizontal line shows 100% reliability, and the bars on each point show the SNR bin width. Note the minimum SNR in source lists is confined to $5\sigma_{\rm rms}$.

pare the GLEAM-300 catalogue measurements to scaled flux densities from GLEAM, GLEAM-X DR2, and GLEAM SGP (scaled from 200 MHz measurements), the VCSS1 (scaled from 340 MHz), WISH (scaled from 352 MHz), and the TGSS ADR1 (scaled from 147.5 MHz). These surveys provide data products that are the reasonably close in sensitivity, resolution, and/or frequency to GLEAM-300. We note that GLEAM-X DR2 and GLEAM SGP inherits a flux density scale from GLEAM, and GLEAM overall is set to the Baars et al. (1977, hereinafter B77) flux density scale. WISH is flux-corrected to the NVSS, which is largely set to the B77 scale as well. For TGSS ADR1, the brightness scale is set to the low-frequency models from Scaife & Heald (2012), tied to the Roger et al. (RCB; 1973) brightness scale. There is an expected $\approx 4\%$ difference between B77 and RCB at these frequencies. VCSS1 is flux-calibrated using Perley & Butler (2017) models for 3C 286 and 3C 138, which again differ by a few percent from the B77 and RCB scales.

For consistency, we take the median α from all crossmatched GLEAM sources (-0.8) to scale all surveys to 300 MHz. During cross-matching we only consider crossmatches within 30 arcsec and only take reasonably compact sources $(S_{\text{int}}/S_{\text{peak}} < 1.2 \text{ in both catalogues, where appropri$ ate) and with no neighbours within 240 arcsec. An Eddington bias (Eddington, 1913) correction is also applied to each catalogue, following equation 4 from Hogg & Turner (1998). Figure 20 shows the scaled flux density ratio $(S_{300}/S_{\text{survey}})$ between the catalogues as a function of the signal-to-noise ratio in the GLEAM-300 catalogue. For comparisons with GLEAM, GLEAM-X DR2, GLEAM SGP, and TGSS ADR1 we see GLEAM-300 flux density measurements are largely in agreement, with average offsets within $\approx 5\%$ for sources above $100\sigma_{\rm rms}$. VCSS1 and WISH flux density comparisons show GLEAM-300 flux densities are $\approx 10\%$ lower, with some additional structure in their distributions.

To estimate the uncertainty in the brightness scale we also cross-match the catalogue to the sky model that was used for calibration and post-imaging brightness scale corrections. From the 84-th percentile of the $>100\sigma_{\rm rms}$ cross-

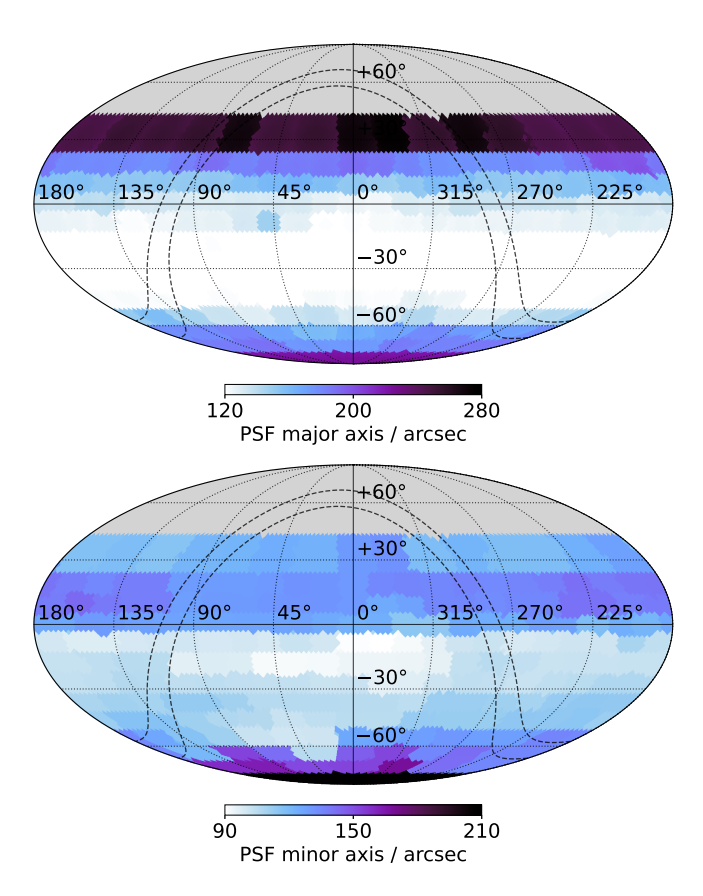


Figure 18. HEALPix representation of the PSF major (*top*) and minor (*bottom*) axes across the sky as recorded at source positions in the catalogue.

Table 2. Brightness scale uncertainty as a function of declination.

Declination range	Brightness scale uncertainty		
$\delta_{ m J2000} < -78.0^{\circ}$	21%		
$-78.0^{\circ} \leq \delta_{\text{J2000}} < -72.0^{\circ}$	16%		
$-72.0^\circ \leq \delta_{ m J2000} < +18.5^\circ$	12%		
+18.5 $^{\circ} \leq \delta_{ extsf{J2000}} \leq$ +24.0 $^{\circ}$	16%		
$\delta_{ m J2000} >$ +24.0 $^\circ$	21%		

matched sources, we suggest an initial brightness scale uncertainty of 9% for declinations covered by the main lobe images $(-78^{\circ} \le \delta_{J2000} \le +24^{\circ})$. For the grating lobe regions $(\delta_{\rm J2000}\,<\,-78^\circ$ and $\delta_{\rm J0000}\,>\,+24^\circ)$ we get $\approx\,13\%$ for the 84-th percentile, though we noted in Section 2.4.3 that the two regions had differences represented by a standard deviation of $\approx 16\%$. To be conservative, we suggest the 16% represents the uncertainty in the brightness scale calibration of the individual snapshots, so consider this the initial brightness scale uncertainty for these regions. These initial uncertainties should be added in quadrature to the GLEAM external brightness scale uncertainty for the relevant declination (see table 4 from Hurley-Walker et al. 2017), except we do not consider the 80% brightness scale uncertainty reported for $\delta_{\rm J2000} < -83.5^{\circ}$ to be necessary here. This yields the full declination-dependent brightness scale uncertainty reported in Table 2, and is included in the catalogue for each source.

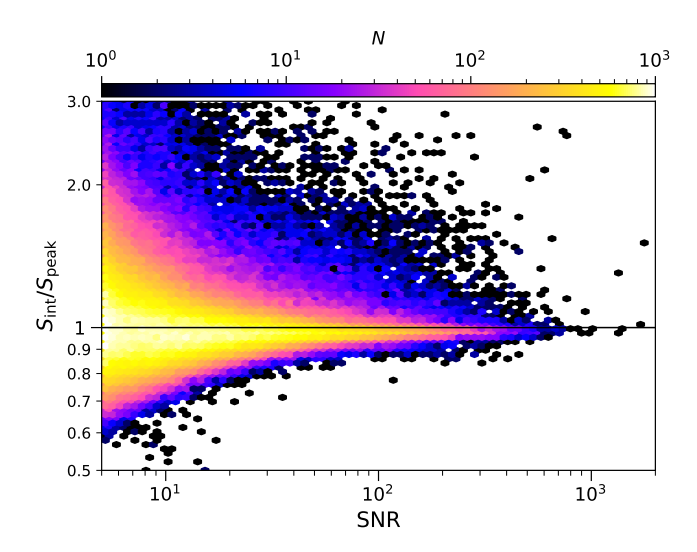


Figure 19. The ratio of $S_{\rm int}/S_{\rm peak}$ as a function of SNR for all sources in the GLEAM-300 catalogue, represented in hexagonal bins. The horizontal line indicates a ratio of 1.

4.6.3 Spectral energy distributions

One of the goals of this work is to provide an additional 'high'frequency data point to GLEAM and/or GLEAM-X measurements to constrain the shapes of source spectral energy distributions (SEDs), particularly in the presence of spectral curvature. As a point of comparison we measure the integrated flux density of Fornax A within a polygon region containing the radio galaxy. We also make the equivalent measurements from the 16 GLEAM SGP mosaics between 107-227 MHz. We compare these GLEAM-300 and GLEAM SGP measurements to the VLA measurements and spectral model from Perley & Butler (2017). The spectral data are shown in Figure 21(i) with the Perley & Butler (2017) logarithmic polynomial model overlaid. The GLEAM-300 data agrees with the VLA measurements and model, though we see some discrepancy between the VLA data and GLEAM SGP data. The SGP data appear to show a steeper overall integrated spectrum for Fornax A. This is likely due to use of robust image weighting combined with a $30-\lambda$ (u, v) cut and 15- λ Tukey taper (corresponding to sensitivity up to ≈ 1.5 deg), so artificial steepening of extended sources is expected, and care should be taken when interpreting spectra in cases of extended sources. Overall, the agreement with the Perley & Butler (2017) suggests the flux density scale (and associated uncertainty) is sensible for the GLEAM-300 data. We do not show a comparison to the original GLEAM as the Fornax A images at some frequencies contain artefacts from the linear mosaic process.

As an example of where the GLEAM-300 datapoint sits within the ecosystem of widefield Southern Sky surveys, we also cross-match GLEAM-300 to GLEAM-X DR2 and the three RACS bands: RACS-low at 887.5 MHz (McConnell et al., 2020; Hale et al., 2021), RACS-mid at 1 367.5 MHz (Duchesne et al., 2023, 2024), and RACS-high at 1 655.5 MHz (Duchesne et al., 2025). We repeat a similar strict multi-matching process employed by Duchesne et al. (2025), which focuses on isolated

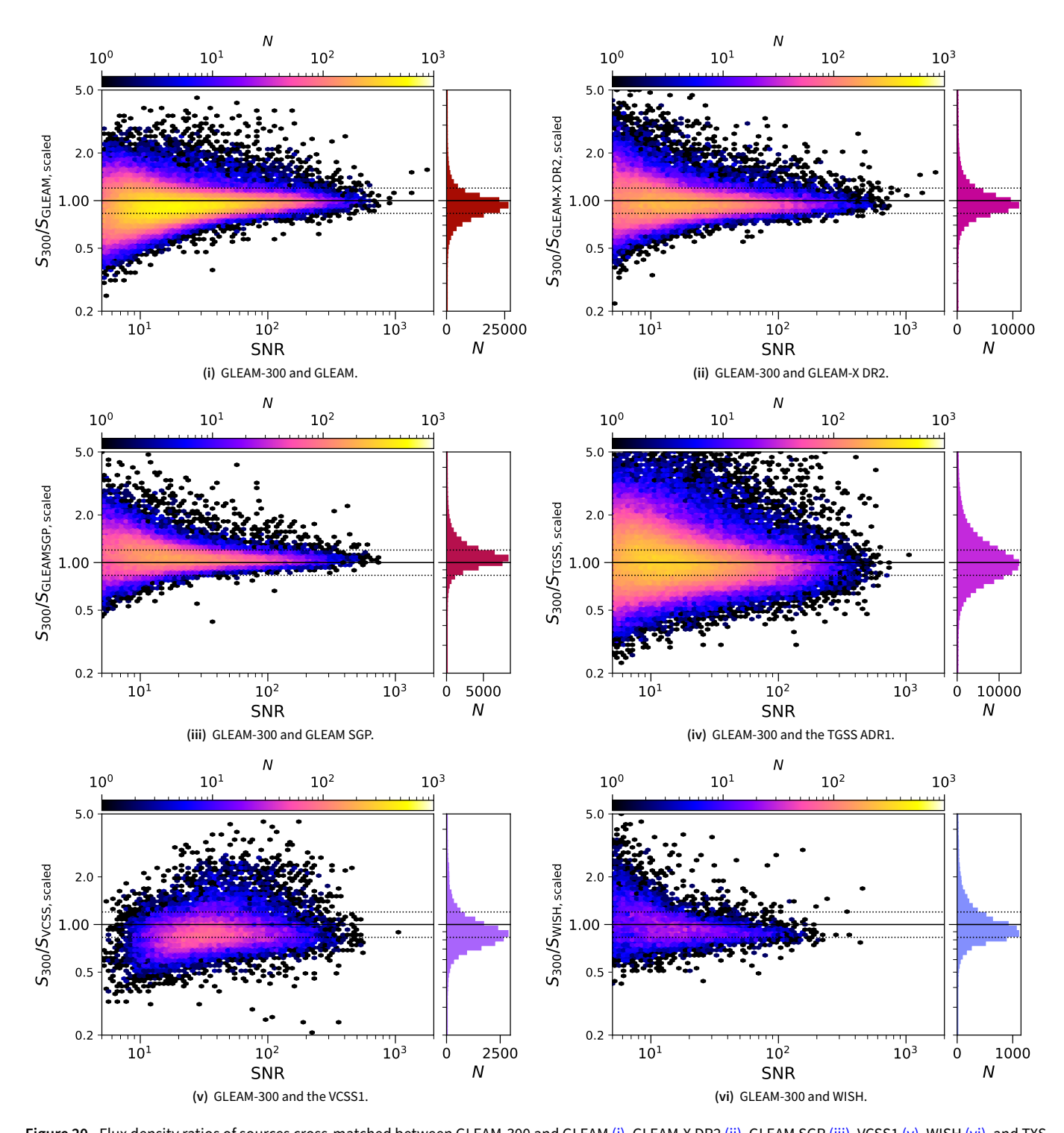


Figure 20. Flux density ratios of sources cross-matched between GLEAM-300 and GLEAM (i), GLEAM-X DR2 (ii), GLEAM SGP (iii), VCSS1 (v), WISH (vi), and TXS (iv), after scaling flux densities to 300 MHz and correcting for Eddington bias, as a function of SNR in the GLEAM-300 catalogue. Solid horizontal line is drawn at 1, and the dashed lines are drawn at \pm 20%. Note the y-axis is scaled logarithmically.

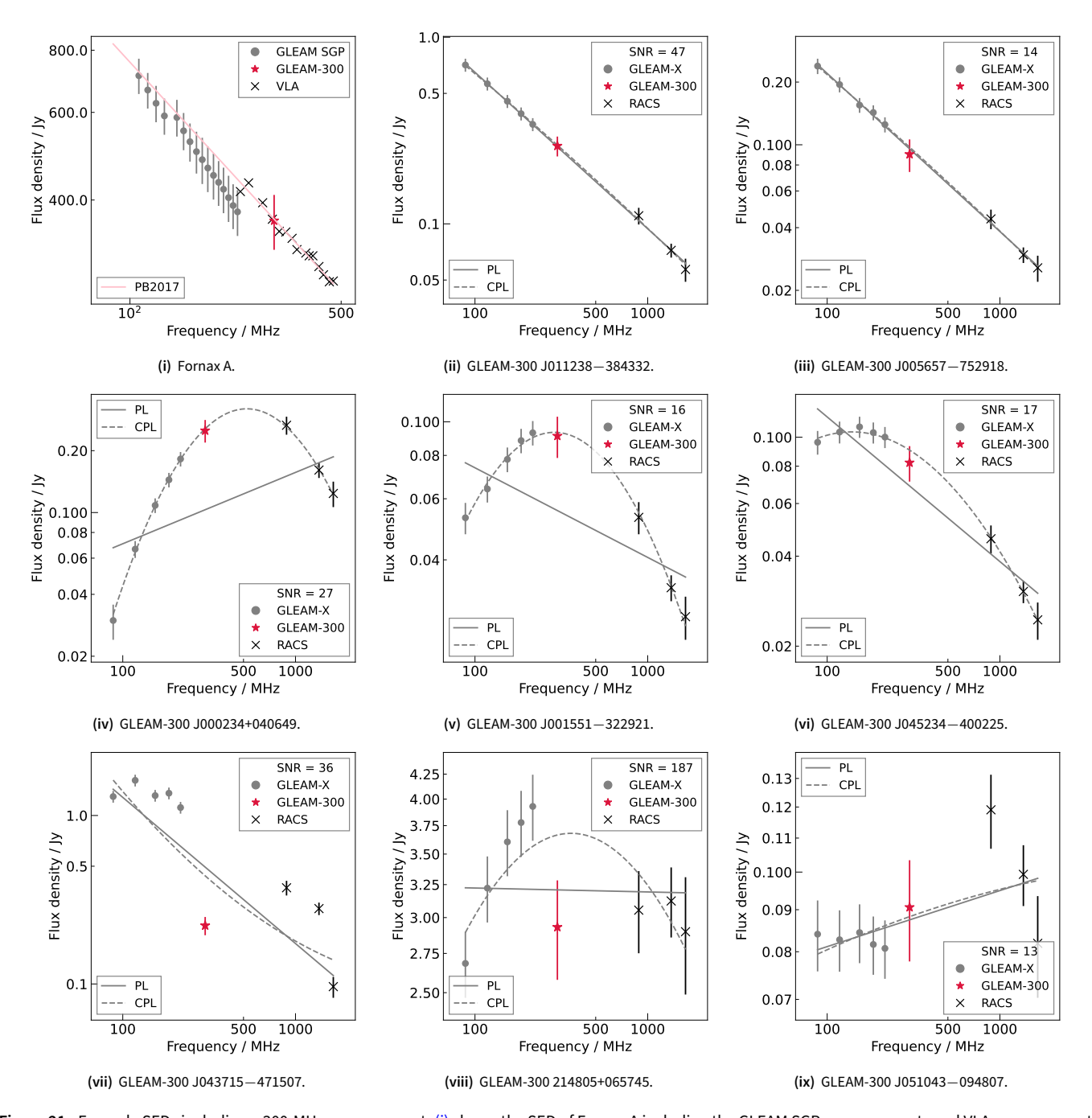


Figure 21. Example SEDs including a 300-MHz measurement. (i) shows the SED of Fornax A including the GLEAM SGP measurements and VLA measurements from Perley & Butler (2017). The fitted logarithmic polynomial model from Perley & Butler (2017) is also shown. (ii)–(iii) show unresolved point sources with standard power law spectra, (iv)–(vi) show curved power law spectra, and (vii)–(ix) comprises variable/flat spectrum sources, all selected after cross-matching the GLEAM-300 catalogue with GLEAM-X DR2 and the RACS catalogues. Power law (PL) and curved power law (CPL) models are fit for illustrative purposes. Note both the x- and y-axes are scaled logarithmically.

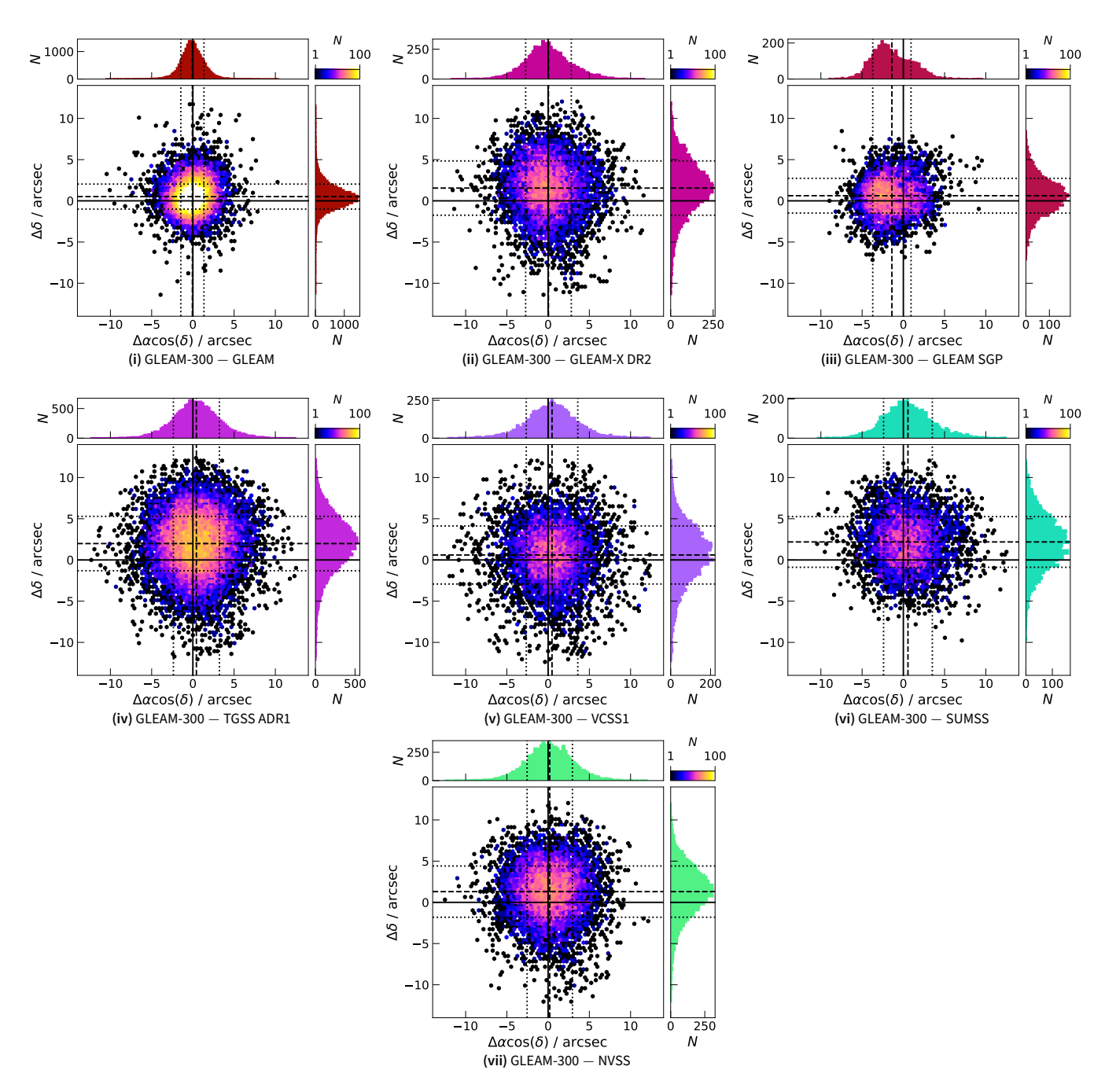


Figure 22. Right ascension (α) and declination (δ) offsets between GLEAM-300 and GLEAM (i), GLEAM-X DR2 (ii), GLEAM SGP (iii), TGSS ADR1 (iv), VCSS1 (v), SUMSS (vi), and the NVSS (vii). Only sources with an SNR > 50 in the GLEAM-300 catalogue are shown. The solid black lines are drawn at 0 offset, the dashed black lines are drawn at the mean offset value, and the dotted black lines are drawn at $\pm 1\sigma$ about the mean offset.

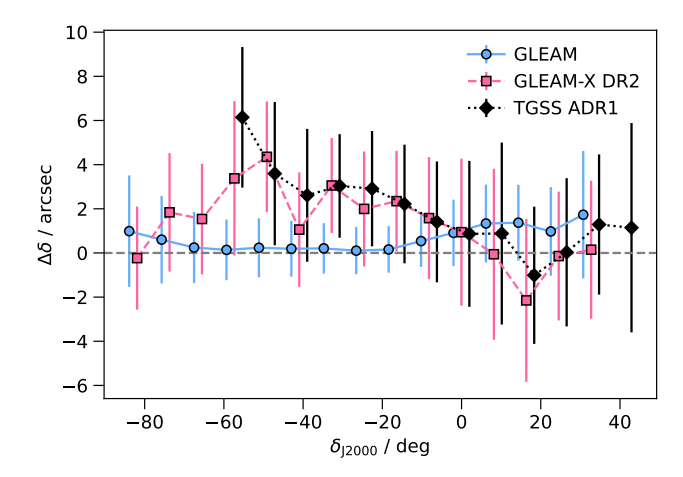


Figure 23. Median-binned declination offsets as a function of declination for cross-matches to GLEAM, GLEAM-X DR2, and TGSS ADR1. The error bars are drawn at $\pm 1\sigma$ for each bin. Bins are offset by 2° for each survey for clarity.

and compact point sources detected above $10\sigma_{\rm rms}$ in all five catalogues under consideration. This choice is to avoid the aforementioned concern with extended source spectra, and to avoid issues arising from differing angular resolution and sensitivities between the surveys. This limits the resultant cross-matched catalogue to 9 880 sources. We then fit generic power law and curved power law models as in e.g. Ross et al. (2024). For the GLEAM-X DR2 data, we opt to use 30-MHz wideband measurements as opposed to 7.68-MHz narrowband measurements for consistency with the GLEAM-300 30-MHz measurement.

Figure 21(ii)-(ix) show a set of example sources with fitted SEDs that include the GLEAM-X, GLEAM-300, and RACS measurements. The sources are selected from the crossmatched sources to showcase a range of spectral morphologies. Figures 21(ii)–(iii) show a selection of sources with standard power law spectra, and Figures 21(iv)–(vi) show example sources with well-modelled curved power law spectra. In addition to the power law and curved spectra, we also show a few examples of more exotic spectra arising from source variability. Figure 21(vii) shows the millisecond pulsar PSR J0437–4715 (Johnston et al., 1993) which was also detected in the MWA circular polarization survey (Lenc et al., 2017). Figure 21(viii) shows a 'flat-spectrum' blazar source, 4C +06.69 (e.g. Healey et al., 2007), and Figure 21(ix) shows NVSS J051042-094813 (Condon et al., 1998), which also has a non-power law spectrum, though we do not explore these sources further here. With the addition of the GLEAM-300 data point, the gap in spectral coverage between GLEAM and RACS (231-888 MHz) is now more accurately filled-in across the whole Southern Sky.

4.7 Astrometry

For assessment of the astrometry, we also cross match the GLEAM-300 catalogue to the SUMSS and the NVSS. We also compare to the other GLEAM catalogues, TGSS ADR1, and VCSS1 again. We consider isolated and compact sources (in each catalogue), and calculate the astrometric offsets as GLEAM-300 — external survey for sources above $50\sigma_{\rm rms}$ in

the GLEAM-300 catalogue. Figure 22 shows the positional offsets in α_{J2000} and δ_{J2000} for the survey comparisons.

As GLEAM is largely used for phase calibration and postimaging astrometric corrections, we see bulk α_{J2000} , δ_{J2000} offsets of -0.006 ± 1.000 and $+0.052 \pm 1.052$, noting that the smallest pixel size in the mosaic images is 17".9 (with a maximum pixel size of 44".6). Other surveys tend towards a bulk offset in declination, up to a few arcsec, with median bulk offsets in δ_{J2000} of +1".55 ± 3".29 for GLEAM-X DR2, +0".60 ± 3".52 for VCSS1, $+1''.99 \pm 3''.30$ for the TGSS ADR1, $+2''.19 \pm 3''.07$ for SUMSS, and $+1.30 \pm 3.11$ for the NVSS. The GLEAM SGP on the other hand features the largest offset in α_{12000} , with $\Delta \alpha \cos \delta = -1.39 \pm 2.32$ along with a marginal offset in δ_{J2000} . GLEAM-X DR2 uses both SUMSS and NVSS for its astrometric corrections so we expect the offsets against SUMSS and NVSS seen by Ross et al. (2024) should be present here too. Of particular note is elongation of the offset distributions towards the lower right of each plot, except in the SUMSS comparison. Figure 23 shows the median-binned declination offsets as a function of declination for the GLEAM, GLEAM-X DR2, and TGSS ADR1 cross-matches. The GLEAM cross-matches deviate in the SCP region and towards the Northern Hemisphere, whereas both the GLEAM-X DR2 and TGSS offsets show similar structure as a function of $\delta_{\rm J2000}$. The GLEAM-300 catalogue has largely inherited an inherent astrometric uncertainty from GLEAM.

5. Applications and future work

5.1 Diffuse and extended radio emission

The GLEAM-300 catalogue provides crucial frequency coverage for understanding the spectral evolution of diffuse non-thermal phenomena in several environments. Both the so-called 'remnants' or 'fossils' associated with switched-off AGN (e.g. Murgia et al., 2011; Quici et al., 2025) and the steep-spectrum radio sources associated with cosmic structures—groups and clusters of galaxies (see e.g. Eckert et al., 2021; van Weeren et al., 2019, respectively)—require broad-band spectral information to understand the physics of the particle acceleration mechanisms at work.

Oftentimes these spectra show significant curvature, such as the remnant radio galaxy NGC 1534 (Duchesne & Johnston-Hollitt, 2019), the 'ultra-steep spectrum jellyfish' associated with Abell 2877 (Hodgson et al., 2021), or the ultra-steep spectrum fossil in Abell 3266 (Duchesne et al., 2022; Riseley et al., 2022). The latter object in particular shows a clear break in the spectrum between 216 MHz (measured by the MWA) and 943 MHz (measured by ASKAP) and constraining the break frequency, as well as the type of break—whether the spectrum is truly curved or shows a sharp break in the injection index, for example—would provide insights into the ageing and evolution of these sources.

Similarly, in cosmic structures such as galaxy groups, bulk motions and interactions in the environment can re-distribute and re-accelerate fossil plasma onto different scales (e.g. Brienza et al., 2022; Candini et al., 2023) but the mechanisms by which this occurs are still poorly understood. The GLEAM-

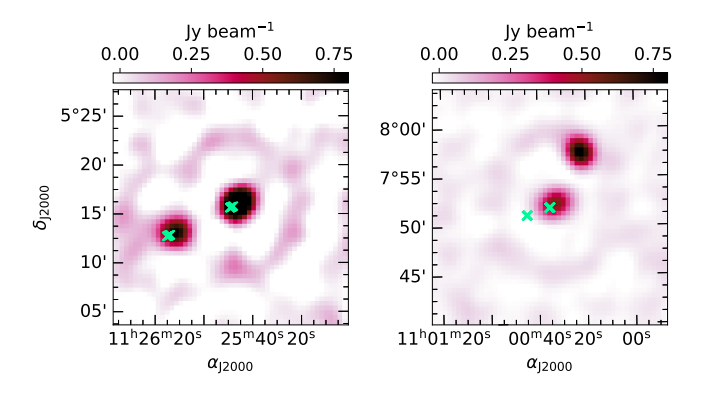


Figure 24. Jupiter detections in the mosaic images. The positions of Jupiter in the individual snapshots are indicated by green crosses, and sources detected at those locations are the weighted-average detection in the mosaic. In the left panel, both radio sources at the marked positions are Jupiter detections. In the right panel, only one source is a Jupiter detection.

300 measurements occupy a critical frequency regime that has been historically served only down to $\delta_{\rm J2000} \approx -53^{\circ}$ (the southern limit of the GMRT); the catalogue published herein significantly broadens the scope of such studies.

Furthermore, the frequency coverage provided by the GLEAM-300 catalogue is essential in supernova remnants (see Dubner & Giacani, 2015, for a recent review) studies which exhibit a variety of spectral behaviours connected to their particle acceleration mechanisms, interactions with the surroundings and energy losses. The GLEAM-300 frequency band is beneficial for identifying turnovers in the spectra at low radio frequencies, which can signify absorption mechanisms such as free-free absorption in ionised gas (e.g. Castelletti et al., 2021), and in particular the 300-MHz data can provide an anchor for the unabsorbed power-law portion of the spectrum at a frequency where interstellar medium (ISM) absorption has not yet taken effect.

The GLEAM-300 data provide a unique opportunity to probe these effects by extending the spectral coverage into an under-explored range. This dataset effectively bridges the very low frequency of GLEAM (72–231 MHz) and the higher frequencies provided by surveys like the Evolutionary Map of the Universe (EMU; Norris et al., 2021; Hopkins et al., 2025) at 944 MHz while awaiting the new SKA infrastructure. Expanding studies of supernova remnants with this catalogue will help constrain the physical processes governing particle acceleration and evolution in these sources.

5.2 Transients and variability

Over the last few years, widefield imaging surveys have become an increasingly popular tool for finding sources that vary on minute- to hour-long time scales, a hitherto relatively unexplored parameter space (e.g. Hyman et al., 2007; Murphy et al., 2013, 2021; Hurley-Walker et al., 2022b). Such surveys can also potentially detect shorter duration (sub-second) events that are sufficient bright (e.g. Wang et al., 2021; Sett et al., 2023; Mcsweeney et al., 2025). The sensitivity of a given survey towards different classes of transient sources is a non-trivial func-

tion of frequency. At lower radio frequencies ($\leq 200 \, \text{MHz}$), detection can be inhibited by higher sky temperatures, intrinsic low-frequency turnovers, as well as the temporal smearing effects of interstellar dispersion and scattering. On the other hand, transient sources' typically steep spectra $(-4 \le \alpha \le -1)$ make detection difficult at higher frequencies ($\gtrsim 1\,\mathrm{GHz}$). This survey, at 300 MHz, may therefore be sensitive to transients that, for one reason or another, are difficult to detect at other frequencies. The individual snapshots have a median noise of $\sigma \approx 68 \,\mathrm{mJy\,beam^{-1}}$; we expect that they will be sensitive to transient events whose brightness (integrated over the two-minute snapshot) is $S_{300} > 5\sigma \approx 340 \,\mathrm{mJy\,beam^{-1}}$. In particular, this survey is likely to detect new long period transients whose single pulses can last anywhere from a few tens of seconds (de Ruiter et al., 2025; Hurley-Walker et al., 2024) to several minutes (Hurley-Walker et al., 2023; Lee et al., 2025). To enable searches of such transients, the individual source lists for each two-minute snapshot are being made available.

We note that Jupiter is detected in snapshots taken on 20–21 February 2016 and 25–26 April 2016 and appears in the mosaic images. The movement across sky over the two nights in February is seen as two separate sources, whereas only a single radio source is seen over the two nights in April. We show the mosaic detections in Figure 24, with green markers indicating the direction of Jupiter in the individual snapshots. Note that Jupiter is not included in the CLEAN mask so has noticeable PSF sidelobes around it. Three sources in the final catalogue are co-located with Jupiter's positions: GLEAM-300 J112611+051306, GLEAM-300 J112546+051601, and GLEAM-300 J110033+075214.

5.3 General data improvements and other additions

One of the limitations of our current GLEAM-300 processing strategy is the lack of consistent in-field calibration. Franzen et al. (2021) highlighted that self-calibration (after initial calibration from other methods) can be used in place of in-field calibration, providing similar results. We find through MWA processing experience that the level of improvement will also depend on the direction being observed and what is in the sky model. Either more consistent in-field calibration or a successful self-calibration procedure would improve the overall sensitivity of the GLEAM-300 survey and reliability at low SNR. At present it is not clear why these processes do not work consistently, though it is likely the combination of inaccurate source models, certain primary beam pointings being more difficult due to attenuated bright sources at the edges of the primary beam lobes, as well as other time/observation-dependent effects such as ionospheric activity.

An interesting avenue for further work in this area will be to develop a linear polarization counterpart to GLEAM-300, akin to the POGS effort at lower MWA frequencies (Riseley et al., 2018, 2020). A detailed understanding of the magnetoionic properties and environments of radio sources requires broadband linear polarization measurements, and the primary figure of merit is complete sampling of a broad range of wavelength-squared (λ^2) coverage. GLEAM-300 now pro-

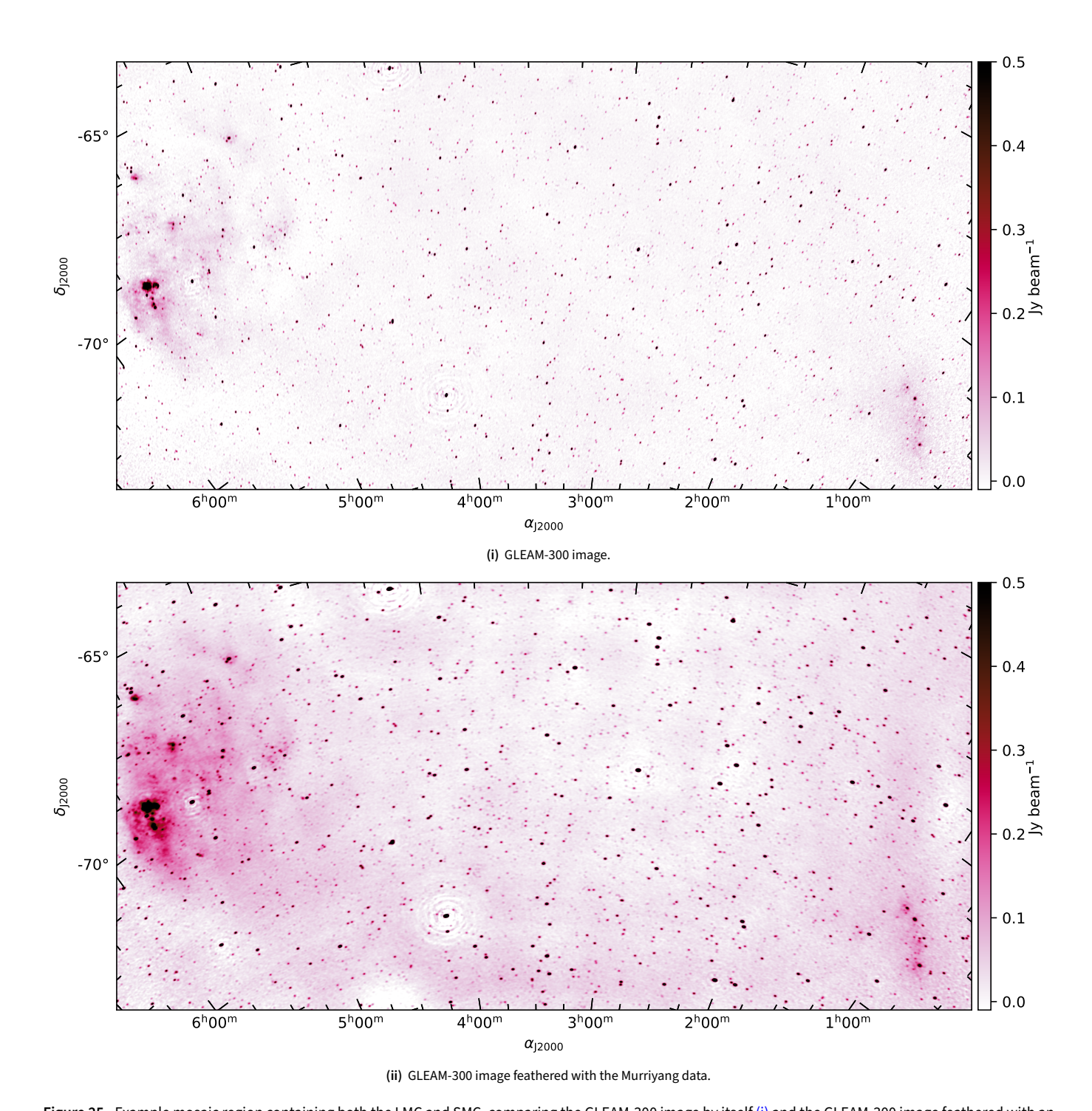


Figure 25. Example mosaic region containing both the LMC and SMC, comparing the GLEAM-300 image by itself (i) and the GLEAM-300 image feathered with an equivalent image from GMIMS-LBS (Wolleben et al., 2019) (ii). The brightness scaling is the same in both panels, and the feathered image highlights additional extended emission within/around both the LMC and SMC as well as Galactic emission in this region.

vides well-understood visibility data from which the required data products—full Stokes continuum cubes—can be produced and analysed. This is however a non-trivial exercise because additional calibration effects require attention, such as XY phase differences, ionospheric Faraday rotation measure corrections, and characterisation and correction of polarization leakage. But the gains can be significant, as a polarization counterpart of GLEAM-300 would help to fill a key gap in λ^2 coverage between POGS and the ASKAP SPICE-RACS catalogue (Thomson et al., 2023) at considerably higher frequency. These intermediate- λ^2 measurements are particularly valuable to understand the details of depolarization effects (see, e.g., Farnsworth et al., 2011) that dramatically reduce the density of linearly polarized sources seen at MWA frequencies compared to GHz-regime observations like those with ASKAP (e.g., O'Sullivan et al., 2023; Piras et al., 2024).

Whilst the focus of this work is on producing a compact source catalogue at 300 MHz, the short baselines of the MWA provide excellent sensitivity to extended diffuse emission from the Milky Way and nearby galaxies. The MWA in the Phase I compact configuration was sensitive to scales of up to ~ 7.4 deg based on the minimum baseline of 7.7 m at 300 MHz. As described in the introduction, GMIMS-LBS (Wolleben et al., 2019) covers the entire GLEAM-300 band and almost the entire survey area (up to $\delta_{J2000} = +20^{\circ}$). Having been observed with Murriyang, a 64 m single dish telescope, GMIMS-LBS can provide the missing 'zero spacings' in GLEAM-300 and provide sensitivity in spatial scales across the entire sky.

By way of example we have combined the GLEAM-300 mosaic of the region surround the LMC and SMC (field 'J0326-72') with GMIMS-LBS using the 'feathering' algorithm (Weiß et al., 2001)^w. We show the original and 'feathered' image in Figure 25, highlighting the additional recovered signal from the large-scale features in the LMC in particular. We intend to combine the entirety of GLEAM-300 with GMIMS-LBS as an enhanced data product in future work.

6. Summary

This work presents a new widefield radio survey conducted by the MWA at the heretofore unexplored frequency band of 300 MHz. The survey, part of the Galactic and Extragalactic MWA All-sky (GLEAM) project and titled GLEAM-300, covers the whole Southern Sky and extends to $\delta_{\rm J2000}\approx +40^{\circ}$. The survey was conducted similarly to other GLEAM surveys, with 2-min snapshot observations taken in declination strips and processed semi-independently prior to mosaicking to increase sensitivity. While no observations directly covered the South Celestial Pole, imaging primary beam grating lobes allowed us to fill in the whole Southern Hemisphere.

The resultant mosaic images have a median angular resolution of 128.8×112.5 and median rms noise of $9.1_{-2.8}^{+5.5}$ mJy beam⁻¹. The brightness scale of the images is reliable to 12-21. A catalogue is constructed from the mosaic images resulting in 338 080 unique Gaussian components

covering the whole survey region. Due to corrections applied to snapshot images, the astrometric accuracy is similar to the original GLEAM, with some bulk offsets up to $\approx 2''$ in declination seen with respect to other surveys, as a function of declination. The overall astrometric accuracy is $\approx 2-4''$.

We also cross-matched a subset of the catalogue to the second data release of GLEAM-X and the three RACS catalogues to illustrate where the 300-MHz measurements sit within the current ecosystem of Southern Sky widefield surveys, and show the overall agreement with the existing data. The 300-MHz datapoint in particular provides a unique measurement in the large spectral gap between previously-published MWA and ASKAP data. This is particularly timely given the ongoing construction of SKA-Low, which will observe from 50-350 MHz. Together with GLEAM and GLEAM-X, this 300 MHz catalogue will provide crucial information for initial calibration and validation of SKA-Low image products in this frequency range. For example, the catalogue is well suited to contribute to the construction of a broadband calibration sky model for SKA-Low, and provides a reference epoch for forthcoming variability studies using SKA-Low data. We release the catalogue and mosaic images to the astronomy community for use in science and data validation work, available at the CSIRO Data Access Portal: https://doi.org/10.25919/z80f-5t62.

Data availability

The GLEAM-300 catalogue and mosaic images are available at the CSIRO Data Access Portal: https://doi.org/10.25919/z80f-5t62.

Much of the code/scripts required to generate plots and other miscellaneous analysis tasks for the GLEAM-300 survey and this manuscript are collected in a python package hosted here: https://gitlab.com/Sunmish/gleam300.

Acknowledgement

The authors would like the thank the anonymous referee for their in-depth reading of the manuscript. Their comments helped improved the work and in particular motivated us to revisit the bias in our original flux density measurements described in Appendix A.

This scientific work uses data obtained from Inyarrimanha Ilgari Bundara / the Murchison Radio-astronomy Observatory. We acknowledge the Wajarri Yamaji People as the Traditional Owners and native title holders of the Observatory site. CSIRO's ASKAP radio telescope is part of the Australia Telescope National Facility (https://ror.org/05qajvd42). Operation of ASKAP is funded by the Australian Government with support from the National Collaborative Research Infrastructure Strategy. ASKAP uses the resources of the Pawsey Supercomputing Research Centre. Establishment of ASKAP, Inyarrimanha Ilgari Bundara, the CSIRO Murchison Radio-astronomy Observatory and the Pawsey Supercomputing Research Centre are initiatives of the Australian Government, with support from the Government of Western Australia and the Science and Industry Endowment Fund.

wImplemented in https://github.com/AlecThomson/FeatherPy.

N.H.-W. is the recipient of an Australian Research Council Future Fellowship (project number FT190100231). CJR acknowledges financial support from the German Science Foundation DFG, via the Collaborative Research Center SFB1491 'Cosmic Interacting Matters – From Source to Signal'.

This research has made use of the VizieR catalogue access tool, CDS, Strasbourg, France (DOI: 10.26093/cds/vizier). The original description of the VizieR service was published in Ochsenbein et al. (2000). We used a range of python software packages during this work and the production of this manuscript, including astropy (Astropy Collaboration et al., 2018), matplotlib (Hunter, 2007), numpy (Harris et al., 2020), scipy (Jones et al., 2001 2017), and healpy (Zonca et al., 2019). We make use of ds9 (Joye & Mandel, 2003), topcat (Taylor, 2005), and the Cube Analysis and Rendering Tool for Astronomy (CARTA; Comrie et al., 2021) for visualisation, as well as the "Aladin sky atlas" developed at CDS, Strasbourg Observatory, France (Bonnarel et al., 2000; Boch & Fernique, 2014) for obtaining catalogue data. For precision rounding we used to-precision: https://bitbucket.org/ william rusnack/to-precision/src/master/. We make use of a selection of colourmaps provided by the cmasher package (van der Velden, 2020), and use https://github.com/eltos/gradient for some colour selections.

References

Arras P., Reinecke M., Westermann R., Enßlin T. A., 2021, A&A, 646, A58 Astropy Collaboration et al., 2018, AJ, 156, 123

Baars J. W. M., Genzel R., Pauliny-Toth I. I. K., Witzel A., 1977, A&A, 61, 99 Becker R. H., White R. L., Helfand D. J., 1995, ApJ, 450, 559

Boch T., Fernique P., 2014, in Manset N., Forshay P., eds, Astronomical Society of the Pacific Conference Series Vol. 485, Astronomical Data Analysis Software and Systems XXIII. p. 277

Bock D. C.-J., Large M. I., Sadler E. M., 1999, AJ, 117, 1578

Bonnarel F., et al., 2000, A&AS, 143, 33

Brienza M., et al., 2022, A&A, 661, A92

Briggs D. S., 1995, PhD thesis, The New Mexico Institute of Mining and Technology, Socorro, New Mexico

CASA Team et al., 2022, PASP, 134, 114501

Candini S., et al., 2023, A&A, 677, A4

Castelletti G., Supan L., Peters W. M., Kassim N. E., 2021, A&A, 653, A62

Clarke T., Kassim N., Polisensky E., Peters W., Giacintucci S., Hyman S. D., 2016, arXiv e-prints, p. arXiv:1603.03080

Comrie A., et al., 2021, CARTA: The Cube Analysis and Rendering Tool for Astronomy, doi:10.5281/zenodo.4905459

Condon J. J., Cotton W. D., Greisen E. W., Yin Q. F., Perley R. A., Taylor G. B., Broderick J. J., 1998, AJ, 115, 1693

Cook J. H., Seymour N., Sokolowski M., 2021, PASA, 38, e063

De Breuck C., Tang Y., de Bruyn A. G., Röttgering H., van Breugel W., 2002, A&A, 394, 59

Douglas J. N., Bash F. N., Bozyan F. A., Torrence G. W., Wolfe C., 1996, AJ, 111, 1945

Dubner G., Giacani E., 2015, A&A Rev., 23, 3

Duchesne S. W., 2021, PhD thesis, Curtin University, Australia, http://hdl. handle.net/20.500.11937/86699

Duchesne S. W., Johnston-Hollitt M., 2019, PASA, 36, e016

Duchesne S. W., Johnston-Hollitt M., Zhu Z., Wayth R. B., Line J. L. B., 2020, PASA, 37, e037

Duchesne S. W., Johnston-Hollitt M., Wilber A. G., 2021, PASA, 38, e031

```
Duchesne S. W., Johnston-Hollitt M., Riseley C. J., Bartalucci I., Keel S. R.,
2022, MNRAS, 511, 3525
```

Duchesne S. W., et al., 2023, PASA, 40, e034

Duchesne S. W., et al., 2024, PASA, 41, e003

Duchesne S. W., et al., 2025, PASA, 42, e038

Eckert D., Gaspari M., Gastaldello F., Le Brun A. M. C., O'Sullivan E., 2021, Universe, 7, 142

Eddington A. S., 1913, MNRAS, 73, 359

Farnsworth D., Rudnick L., Brown S., 2011, AJ, 141, 191

Franzen T. M. O., Hurley-Walker N., White S. V., Hancock P. J., Seymour N., Kapińska A. D., Staveley-Smith L., Wayth R. B., 2021, PASA, 38, e014

Górski K. M., Hivon E., Banday A. J., Wandelt B. D., Hansen F. K., Reinecke M., Bartelmann M., 2005, ApJ, 622, 759

Hale C. L., et al., 2021, PASA, 38, e058

Hancock P. J., Murphy T., Gaensler B. M., Hopkins A., Curran J. R., 2012, MNRAS, 422, 1812

Hancock P. J., Trott C. M., Hurley-Walker N., 2018, PASA, 35, e011

Harris C. R., et al., 2020, Nature, 585, 357

Healey S. E., Romani R. W., Taylor G. B., Sadler E. M., Ricci R., Murphy T., Ulvestad J. S., Winn J. N., 2007, ApJS, 171, 61

Hodgson T., Bartalucci I., Johnston-Hollitt M., McKinley B., Vazza F., Wittor D., 2021, ApJ, 909, 198

Hogg D. W., Turner E. L., 1998, PASP, 110, 727

Hopkins A., et al., 2025, PASA, 42, e071

Hotan A. W., et al., 2021, PASA, 38, e009

Hunter J. D., 2007, Computing in Science and Engineering, 9, 90

Hurley-Walker N., Hancock P. J., 2018, Astronomy and Computing, 25, 94

Hurley-Walker N., et al., 2017, MNRAS, 464, 1146

Hurley-Walker N., et al., 2019, PASA, 36, e047

Hurley-Walker N., et al., 2022a, PASA, 39, e035

Hurley-Walker N., et al., 2022b, Nature, 601, 526

Hurley-Walker N., et al., 2023, Nature, 619, 487

Hurley-Walker N., et al., 2024, ApJ, 976, L21

Hyman S. D., Roy S., Pal S., Lazio T. J. W., Ray P. S., Kassim N. E., Bhatnagar S., 2007, ApJ, 660, L121

Intema H. T., Jagannathan P., Mooley K. P., Frail D. A., 2017, A&A, 598, A78 Johnston S., et al., 1993, Nature, 361, 613

Jones E., Oliphant T., Peterson P., et al., 2001–2017, SciPy: Open source scientific tools for Python, http://www.scipy.org/

Jordan C. H., et al., 2025, in URSI Asia-Pacific Radio Science Conference. URSI, doi:10.46620/ursiaprasc25/lscn1310.

Jorsater S., van Moorsel G. A., 1995, AJ, 110, 2037

Joye W. A., Mandel E., 2003, in Payne H. E., Jedrzejewski R. I., Hook R. N., eds, Astronomical Society of the Pacific Conference Series Vol. 295, Astronomical Data Analysis Software and Systems XII. p. 489

Knowles K., et al., 2022, A&A, 657, A56

Lane W. M., Cotton W. D., van Velzen S., Clarke T. E., Kassim N. E., Helmboldt J. F., Lazio T. J. W., Cohen A. S., 2014, MNRAS, 440, 327

Large M. I., Mills B. Y., Little A. G., Crawford D. F., Sutton J. M., 1981, MNRAS, 194, 693

Lee Y. W. J., et al., 2025, Nature Astronomy, 9, 393

Lenc E., et al., 2017, PASA, 34, e040

Lenc E., Murphy T., Lynch C. R., Kaplan D. L., Zhang S. N., 2018, MNRAS, 478, 2835

Lynch C. R., et al., 2021, PASA, 38, e057

Mauch T., Murphy T., Buttery H. J., Curran J., Hunstead R. W., Piestrzynski B., Robertson J. G., Sadler E. M., 2003, MNRAS, 342, 1117

McConnell D., et al., 2020, PASA, 37, e048

Mcsweeney S. J., Moseley J., Hurley-Walker N., Grover G., Horváth C., Galvin T. J., Meyers B. W., Tan C. M., 2025, ApJ, 981, 143

Mohan N., Rafferty D., 2015, PyBDSF: Python Blob Detection and Source Finder (ascl:1502.007)

Murgia M., et al., 2011, A&A, 526, A148

```
Murphy T., Mauch T., Green A., Hunstead R. W., Piestrzynska B., Kels A. P.,
  Sztajer P., 2007, MNRAS, 382, 382
Murphy T., et al., 2013, PASA, 30, e006
Murphy T., et al., 2021, PASA, 38, e054
Norris R. P., et al., 2021, PASA, 38, e046
O'Sullivan S. P., et al., 2023, MNRAS, 519, 5723
Ochsenbein F., Bauer P., Marcout J., 2000, A&AS, 143, 23
Offringa A. R., Smirnov O., 2017, MNRAS, 471, 301
Offringa A. R., van de Gronde J. J., Roerdink J. B. T. M., 2012, A&A, 539,
   A95
Offringa A. R., et al., 2014, MNRAS, 444, 606
Offringa A. R., et al., 2015, PASA, 32, e008
Ott J., Walter F., Brinks E., Van Dyk S. D., Dirsch B., Klein U., 2001, AJ, 122,
Perley R. A., Butler B. J., 2017, ApJS, 230, 7
Peters W., Polisensky E., Brisken W., Cotton W., Clarke T., Giacintucci S.,
   Kassim N., 2021, in American Astronomical Society Meeting Abstracts. p.
   211.06
Peters W., Clarke T., Giacintucci S., Nyland K., Polisensky E., 2022, The
   VLITE Commensal Sky Survey (VCSS) Epoch 1 Bright Catalog Re-
   lease, https://ws.cadc-ccda.hia-iha.nrc-cnrc.gc.ca/files/vault/cirada/VCSS
   Catalogue/VCSS_Bright_Catalog_Memo.pdf
Piras S., et al., 2024, A&A, 687, A267
Polisensky E., et al., 2016, ApJ, 832, 60
Quici B., Turner R. J., Seymour N., Hurley-Walker N., 2025, MNRAS, 537,
Radcliffe J. F., Beswick R. J., Thomson A. P., Njeri A., Muxlow T. W. B., 2024,
  MNRAS, 527, 942
Riseley C. J., et al., 2018, PASA, 35, e043
Riseley C. J., et al., 2020, PASA, 37, e029
Riseley C. J., et al., 2022, MNRAS, 515, 1871
Roger R. S., Costain C. H., Bridle A. H., 1973, AJ, 78, 1030
Ross K., et al., 2024, PASA, 41, e054
Scaife A. M. M., Heald G. H., 2012, MNRAS, 423, L30
Schwarz G., 1978, Annals of Statistics, 6, 461
Sett S., Bhat N. D. R., Sokolowski M., Lenc E., 2023, PASA, 40, e003
Smirnov O. M., 2011, A&A, 527, A107
Sokolowski M., Wayth R. B., Lewis M., 2016, arXiv e-prints, p.
   arXiv:1610.04696
Sokolowski M., et al., 2017, PASA, 34, e062
Sokolowski M., et al., 2020, PASA, 37, e021
Taylor M. B., 2005, in Shopbell P., Britton M., Ebert R., eds, Astronomical So-
  ciety of the Pacific Conference Series Vol. 347, Astronomical Data Analysis
   Software and Systems XIV. p. 29
Thomson A. J. M., et al., 2023, PASA, 40, e040
Tingay S. J., et al., 2013, PASA, 30, e007
Wang Z., et al., 2021, ApJ, 920, 45
Wayth R. B., et al., 2015, PASA, 32, e025
Wayth R. B., et al., 2018, PASA, 35, e033
Weiß A., Neininger N., Hüttemeister S., Klein U., 2001, A&A, 365, 571
White R. L., Becker R. H., Helfand D. J., Gregg M. D., 1997, ApJ, 475, 479
Wolleben M., et al., 2019, AJ, 158, 44
Ye H., Gull S. F., Tan S. M., Nikolic B., 2022, MNRAS, 510, 4110
Zonca A., Singer L., Lenz D., Reinecke M., Rosset C., Hivon E., Gorski K.,
  2019, The Journal of Open Source Software, 4, 1298
de Ruiter I., et al., 2025, Nature Astronomy, 9, 672
van Weeren R. J., de Gasperin F., Akamatsu H., Brüggen M., Feretti L., Kang
   H., Stroe A., Zandanel F., 2019, Space Sci. Rev., 215, 16
```

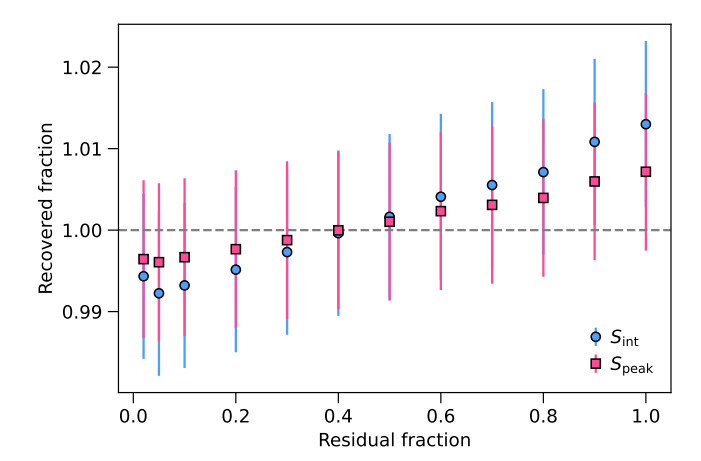


Figure A1. Recovered integrated (S_{int}) and peak flux densities (S_{peak}) as measured by aegean for a simulated source at varying CLEAN depths. The y-axis shows the recovered fraction of the measurement and the x-axis shows the fraction of the measured emission that is composed of residual, 'un-CLEAN' emission. The uncertainties are those reported by aegean from model fitting only. A residual fraction of 1 indicates no CLEANing done.

A. Faint source measurement bias

In initial processing and subsequent assessment of the brightness scale of the GLEAM-300 catalogue, we noticed low-SNR sources were systematically fainter when compared to other catalogues. We first cross-matched the source-lists from each 300-MHz mosaic to the GLEAM catalogue, considering isolated and near-compact sources to assess the individual mosaics prior to combining the source list to make the contiguous catalogue. Despite having similar sensitivities, we also corrected for Eddington bias (Eddington, 1913) for the GLEAM-300 and GLEAM catalogue measurements, following equation 4 from Hogg & Turner (1998). We found an offset in the lowest SNR bins of ≈ 29 mJy, though it varied as a function of source brightness. This offset was also present for comparisons with any surveys that reach or exceed the sensitivity of GLEAM-300 so pointed to an intrinsic bias within our data. We explore this issue and detail the resolution in the following sections.

A.1 The effect of shallow CLEANing?

Snapshot images are cleaned to a depth of, at best, $1\sigma_{rms}$, where σ_{rms} is a position-independent measure. The typical σ_{rms} in the 2-min snapshots is $\approx 68\, \rm mJy\, beam^{-1}$ (Table 1). The final mosaic images approach a median $\sigma_{rms} \approx 9\, \rm mJy\, beam^{-1}$ (see Section 4.3). This results in residual 'un-CLEANed' emission in the mosaic images that becomes significant and does not have the same PSF as the restored images. When there is a significant difference between the area of the fitted 2-D Gaussian restoring beam and the original PSF, the measured flux densities of low-SNR sources can be incorrect (e.g. Jorsater & van Moorsel, 1995; Ott et al., 2001; Duchesne et al., 2021; Radcliffe et al., 2024).

To check this effect on our data, we perform a test on a simulated arbitrary brightness point source injected into an example snapshot dataset with typical (u,v) coverage, and perform CLEANing to various depths (including no CLEANing

van der Velden E., 2020, The Journal of Open Source Software, 5, 2004

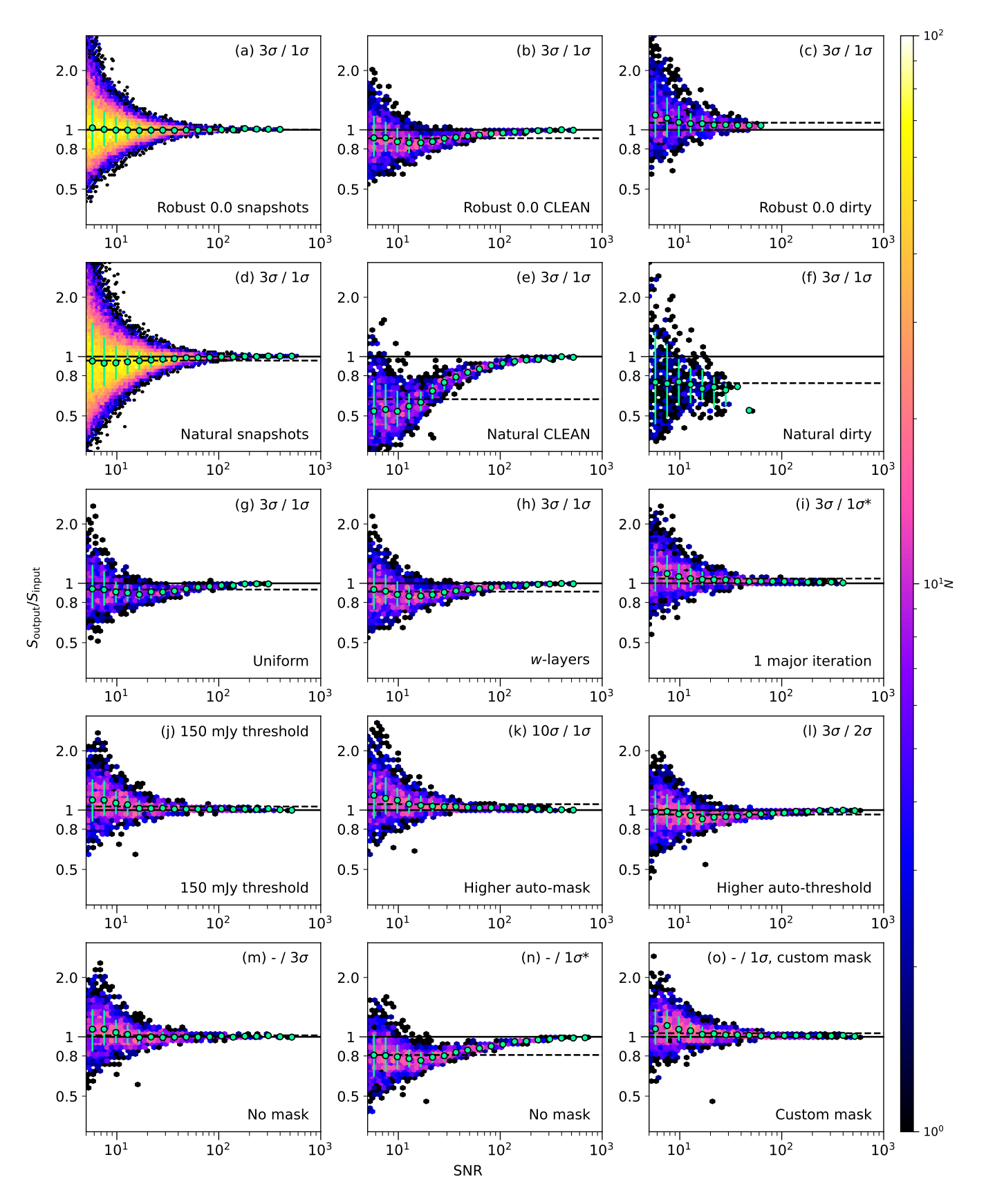


Figure A2. Recovered flux density (as $S_{\text{output}}/S_{\text{input}}$) as a function of SNR ($S_{\text{output},\text{peak}}/\sigma_{\text{rms}}$) in simulated data for the J1234–27 mosaic for a range imaging setups. Green markers indicate medians within SNR bins with associated 16-th and 84-th percentiles. The solid black line indicates a ratio of 1, and the dashed black line indicates the overall median for a given test. CLEAN depth stopping thresholds supplied to WSClean are recorded in the top right of each panel (either a fixed value or as auto-mask / auto-threshold). A '*' next to a threshold label indicates the real stopping threshold is larger than this value due to major or minor iteration limits. Note the difference in sensitivity between snapshots and mosaics is approximately a factor of ten.

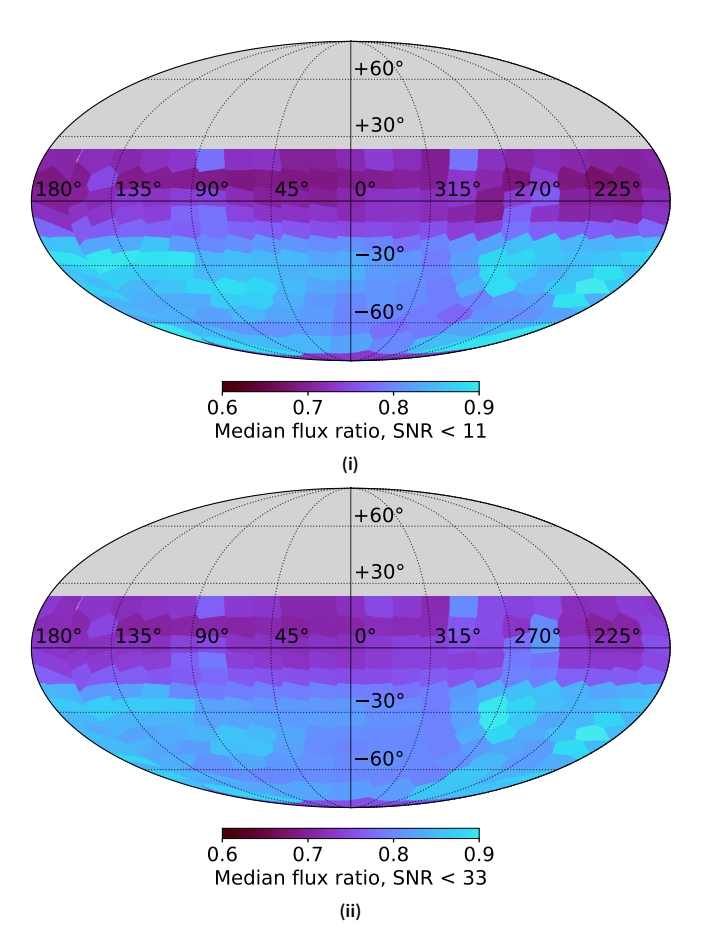


Figure A3. Interpolated, HEALPix-binned maps showing the median flux density ratio $(S_{\text{output}}/S_{\text{input}}$ for simulated mosaics after imaging with automatic masking and thresholding of 3 and 1, respectively. We show the medians for sources with SNR < 11 (i) and sources with SNR < 33 (ii), corresponding to the two approximate CLEAN depths.

at all, but assuming a 2-D Gaussian fitted beam). We measure the final integrated and peak flux densities using <code>aegean</code>, with resulting measurements shown in Figure A1. We see variation in the measured integrated and peak flux densities of up to $\approx 2\%$, though within the fitting uncertainties reported by <code>aegean</code> and so are not likely to be a significant effect for these data.

A.2 The effect of deep CLEANing?

Duchesne et al. (2020) describes a bias observed in stacked MWA images that reduces the flux density of sources as a function of signal-to-noise ratio (SNR). This effect is only noticeable in the final stacked images, and presents similar to the CLEAN bias described by Becker et al. (1995) (see also White et al., 1997; Condon et al., 1998), and Duchesne et al. (2020) assumed it was the same effect. CLEAN bias results in a reduction of peak flux density by a constant amount for all sources, which therefore affects fainter sources more severely. To assess any technical issues arising from CLEAN, imaging, or stacking (and to avoid any inherent biases within external catalogues such as GLEAM), we created simulated snapshot images and mosaics using a simple sky model based on the real

Table A1. List of sources subtracted when outside an image FoV.

Source	$lpha_{J2000}$	δ_{J2000}	$S_{300\mathrm{MHz}}$ a
	(hh:mm:ss)	(dd:mm:ss.s)	(Jy)
3C 123	04:37:04	+29:40:13.8	140
3C 161	06:27:10	-05:53:05.0	59
3C 353	17:20:28	-00:58:47.0	200
3C 409	20:14:28	+23:34:53.0	69
3C 444	22:14:32	-17:01:39.0	49
Cassiopeia A	23:23:28	+58:48:42.0	9900
Centaurus A	13:25:14	-43:12:59.2	3200
Centaurus B	13:46:49	-60:24:12.6	110
Cygnus A	19:59:24	+40:43:52.1	3700
Fornax A	03:22:45	-37:12:43.9	460
Hercules A	16:51:17	+04:59:23.5	200
Hydra A	09:18:05	-12:03:45.8	160
Pictor A	05:19:50	-45:45:50.9	200
Taurus A	05:34:33	+22:01:37.8	1000
Virgo A	12:30:48	+12:22:01.9	280
NGC 253	00:47:37	-25:17:09.4	13
PKS 0408-65	04:08:20	-65:45:09.1	57
PKS 0410-75	04:08:48	-75:07:19.3	31
PKS 0420-62	04:20:56	-62:23:33.5	17
PKS 0442-28	04:44:37	-28:09:47.2	26
PKS 0521-36	05:22:58	-36:27:30.8	47
PKS 1610-60	16:15:05	-60:56:13.9	100
PKS 1932-46	19:35:56	-46:20:38.7	52
PKS 2153-69	21:57:06	-69:41:24.0	88
PKS 2331-41	23:34:26	-41:25:24.0	20
PKS 2356-61	23:59:03	-60:55:11.0	62
PMN J1607-6331	16:06:39	-63:29:56.2	10
Galactic Centre	17:45:43	-28:58:04.5	390

a Expected flux density at 300 MHz based on the input models.

300 MHz catalogue.

A.2.1 Simulating snapshot images

We use $mwa_hyperdrive^x$ (Jordan et al., 2025) to simulate the visibilities, which makes use of the snapshot metadata file to simulate the visibilities as they were observed. The snapshots are simulated at their original time resolution (0.5 s) and then averaged to 4 s after injecting the local sky model.

For the sky model we use our initial 300-MHz catalogue. We remove sources if they have neighbours within 240 arcsec (corresponding to approximately the largest PSF in the catalogue), and for the purpose of the simulation assume all sources are point sources—this is to aid in cross-matching to the model catalogue once the images are made and to avoid other issues relating to source-finding/characterisation of extended sources. We construct a local apparent brightness sky model for each snapshot observation, restricted to sources within the output image bounds. The source brightness is attenuated across four

xhttps://github.com/MWATelescope/mwa_hyperdrive.

specific frequencies within the band that are modelled by the FEE primary beam model.

We also inject noise into the visibilities, which is assumed to be Gaussian and to have a standard deviation of 600 Jy for the real and imaginary parts of the complex visibility. This generates $\approx 50\, \rm mJy\, beam^{-1}$ rms noise in the output snapshot images which approximately corresponds to the median rms noise we see in the real snapshots. We note this does not include flagging, real calibration errors, baseline/antenna-dependent noise, the effects of the ionosphere, or other real noise sources in the signal chain.

The snapshots are then imaged using our original imaging parameters. Namely, we use WSClean with a auto-masking threshold of $3\sigma_{\rm rms}$ and an auto-threshold of $1\sigma_{\rm rms}$. The images are then primary-beam corrected and we use aegean for source-finding on each snapshot with a detection threshold of $5\sigma_{\rm rms}$. Simulated (and real) snapshots usually have around 200 sources detected above $5\sigma_{\rm rms}$, but approximately 4 000–5 000 are injected into each visibility dataset.

A.2.2 Testing the snapshots and mosaics

For the initial set of tests, we focus on a mosaic region centered on $(\alpha_{\rm J2000}, \delta_{\rm J2000}) = (12^{\rm h}34^{\rm m}, -27^{\rm d}00^{\rm m})$, using 343 snapshots taken near zenith. We create the simulated mosaic using the simulated snapshot images following the process used for the real data. We run source-finding on each simulated snapshot and the resultant mosaic and cross-match to our input model and look at the ratio of the measured flux density in the simulated mosaic ($S_{\rm output}$) compared to the input model ($S_{\rm input}$). We also repeat the mosaicking and source-finding on the images without deconvolution (i.e. the 'dirty' images), assuming the same restoring beam in the final images $^{\rm y}$.

Figure A2(a)–(c) shows the results of the simulated dataset with the original imaging parameters, with the flux density ratios ($S_{
m output}/S_{
m input}$) as a function of SNR for the snapshot source lists [Figure A2(a)], the simulated mosaic [Figure A2(b)], and the simulated dirty mosaic [Figure A2(c)]. We see that the snapshot source lists (for sources above $5\sigma_{\rm rms}$) do not immediately show any discrepancy. The simulated mosaic shows the bias, and the simulated dirty mosaic conversely shows the opposite with $S_{\text{output}}/S_{\text{input}} > 1$, but with larger scatter. We apply a correction for Eddington bias, so we do not expect an increase in S_{output} for low-SNR sources. We note there is no significant difference between integrated and peak flux densities in the simulated data. For the first epoch VCSS data, Peters et al. (2022) found a difference in the integrated and peak flux density measurements as a function of SNR that they note could be a result of blurring from astrometric offsets between images when making mosaics. That is not likely a significant effect here.

As well as the normal imaging and mosaicking setup, to aid in understanding where the bias arises we perform a series of similar simulations with some modification to imaging or mosaicking parameters. These test are summarised as follows:

- Primary beam as weight. We normally use a positiondependent rms noise map for mosaic weighting. We construct a mosaic using primary beam weights instead, though this produces the same results as expected as the smoothly varying noise maps largely trace the primary beam attenuation pattern.
- 2. Natural and uniform image weighting. We repeat the imaging and mosaicking process for all snapshots natural weighting [Figure A2(d)–(f)] and with uniform weighting [panel (g)]. For natural weighting, the effect becomes more significant, and we begin to see the effect in the individual snapshots as well. Natural weighting may also show the effect described in Appendix A.1. Conversely, uniform weighting reduces the effect somewhat.
- 3. *w-snapshot gridding*. We test the original widefield gridder implemented in WSClean. The result for the CLEAN mosaic is shown in Figure A2(h), and is identical to the *w*-gridder case.
- 4. One major iteration during deconvolution. We restrict CLEAN to one major iteration, which in practice CLEANs to $\approx 3\sigma_{\rm rms}$. In this case bright sources are well-recovered, with fainter sources tracing the dirty mosaic (due to lack of deconvolution). While snapshots look the same with less CLEANing, the mosaic image quality is noticeably worse with obvious residual sidelobes around sources. The result is shown in Figure A2(i).
- 5. Fixed 150-mJy threshold. We use a fixed 150-mJy threshold ($\approx 3\sigma_{\rm rms}$) which returns the same result as using one major iteration as they CLEAN to similar depths. The result is shown on Figure A2(j).
- 6. Varying auto-mask and auto-threshold levels. We test $10\sigma_{\rm rms}$ / $1\sigma_{\rm rms}$ [Figure A2(k)] and $3\sigma_{\rm rms}$ / $2\sigma_{\rm rms}$ [Figure A2(l)] auto-mask / auto-threshold levels. The higher auto-mask level again returns the same result as the fixed threshold and single major iteration. $3\sigma_{\rm rms}$ / $2\sigma_{\rm rms}$ begins to show the bias.
- 7. No CLEAN masking. We test $3\sigma_{rms}$ [Figure A2(m)] and $1\sigma_{rms}$ [Figure A2(n)] automatic thresholds without masks. $3\sigma_{rms}$ is effectively repeating previous tests with almost identical results. In the $1\sigma_{rms}$ case, the effective CLEAN depth is only $\approx 2\sigma_{rms}$ as the minor iteration limit (250 000) is reached first. The $1\sigma_{rms}$ threshold yields the worst results, highlighting the importance of the mask when CLEANing into the noise.
- 8. Custom mask around known sources. Finally, we construct a custom CLEAN mask using 3×3 pixel boxes placed at the location of simulated sources and CLEAN to an automatic $1\sigma_{rms}$ threshold. The result is shown on Figure A2(o)—this removes the bias, suggesting the normal auto-masking process is not adequate for our use-case and in combination with other imaging parameters.

To assess the effect over the whole survey, we repeated

^yAs noted in Section A.1, we do not expect the integrated volume of the synthesised beam to differ much from the fitted 2-D Gaussian beam in the restored/CLEANed images for robust 0.0 image weighting, though for different image weightings with different PSFs this may be the case. In particular, the naturally weighted data shown in Figure A2 features an additional offset in the flux density recovery for sources that are not deconvolved and may be a result of PSF area differences.

the initial simulation process for all of the original mosaics, including $\approx 14\,000$ snapshots. Figure A3 shows the median ratio of $S_{\text{output}}/S_{\text{input}}$ after interpolation and HEALPix binning for the 242 mosaic regions. We show this for sources with SNR < 11 [Figure A3(i)] and SNR < 33 [Figure A3(ii)], separately, corresponding to the two CLEAN thresholds used by WSClean. In general, there is further reduction of flux density recovery beyond SNR = 33, but there is some flattening of the reduction beyond this initial CLEAN masking threshold. We note also clear variation as a function of declination, with $\delta_{\rm J2000} > -26.7^{\circ}$ regions showing the largest reduction in recovered flux density, generally. Some variation as a function of position can be attributed to the difference in the numbers of sources for each mosaic region, as we only simulate sources that are reported in the final catalogue. While the PSF tends to be larger at high declination and for the SCP region, the flux density does not appear to reduce as a function of the overall Gaussian PSF size. Similarly, source density does not appear to correlate with flux density bias in the simulated mosaics.

The result of the tests highlights the importance of a carefully constructed mask when CLEANing below $3\sigma_{\rm rms}$ (i.e. into the noise). We conclude that the auto-masking with our other imaging parameters (including iteration limits and rms calculations for thresholding) are resulting in over-CLEANing. While our initial attempt at resolving this issue was to derive corrections based on these simulated data, because the effect varies significantly as a function of position we found the postimaging corrections to not be as effective as simply re-imaging with modified imaging parameters. To reduce this effect, we suggest either higher CLEAN thresholds or more careful masking. We opted for both, since imaging stages for these data are relatively cheap computationally compared to other processing stages—e.g. flagging and off-axis source subtraction take a majority of the processing time and needs to be redone when re-imaging as we do not store calibrated MeasurementSets.

B. Subtracted sources

As described in Section 2.2, we subtract or peel a selection of bright sources when they appear above 2.3 Jy and 77 Jy in apparent brightness, respectively, in a given observation when outside of the imaged FoV. As they are only subtracted when outside of the imaged FoV, they remain in the mosaics and are therefore included in the catalogue. The complete collection of subtracted sources is summarised in Table A1 with model absolute 300-MHz total flux densities. Models are a compilation from those used by general MWA continuum processing (e.g. Hurley-Walker et al., 2017; Duchesne et al., 2020; Duchesne, 2021; Franzen et al., 2021), including a new model of a portion of the Galactic Centre which was constructed by running PyBDSF (Mohan & Rafferty, 2015) on initial GLEAM-300 mosaic images to generate 2-D Gaussian components.